

# A deep, high resolution survey of the low frequency radio sky

E. Lenc

*Centre for Astrophysics and Supercomputing, Swinburne University of Technology, Mail number H39, P.O. Box 218, Hawthorn, Victoria 3122*

`elenc@astro.swin.edu.au`

M.A. Garrett<sup>1</sup>

*Netherlands Foundation for Research in Astronomy (ASTRON), Postbus 2, 7990 AA Dwingeloo, The Netherlands*

`garrett@astron.nl`

O. Wucknitz<sup>2</sup>, J.M. Anderson

*Joint Institute for VLBI in Europe, Postbus 2, 7990 AA Dwingeloo, The Netherlands*

`wucknitz@jive.nl, anderson@jive.nl`

and

S.J. Tingay

*Department of Imaging and Applied Physics, Curtin University of Technology, Bentley 6845, Western Australia, Australia*

## ABSTRACT

We report on the first wide-field, very long baseline interferometry (VLBI) survey at 90 cm. The survey area consists of two overlapping 28 deg<sup>2</sup> fields centred on the quasar J0226+3421 and the gravitational lens B0218+357. A total of 618 sources were targeted in these fields, based on identifications from

---

<sup>1</sup>Adjunct Professor, Centre for Astrophysics and Supercomputing, Swinburne University of Technology, Mail number H39, P.O. Box 218, Hawthorn, Victoria 3122

<sup>2</sup>Argelander-Institut für Astronomie, Universität Bonn, Auf dem Hügel 71, 53121, Bonn, Germany; `wucknitz@astro.uni-bonn.de`

Westerbork Northern Sky Survey (WENSS) data. Of these sources, 272 had flux densities that, if unresolved, would fall above the sensitivity limit of the VLBI observations. A total of 27 sources were detected as far as  $2^\circ$  from the phase centre. The results of the survey suggest that at least 10% of moderately faint ( $S \sim 100$  mJy) sources found at 90 cm contain compact components smaller than  $\sim 0.1$  to  $0.3$  arcsec and stronger than 10% of their total flux densities. A  $\sim 90$  mJy source was detected in the VLBI data that was not seen in the WENSS and NRAO VLA Sky Survey (NVSS) data and may be a transient or highly variable source that has been serendipitously detected. This survey is the first systematic (and non-biased), deep, high-resolution survey of the low-frequency radio sky. It is also the widest field of view VLBI survey with a single pointing to date, exceeding the total survey area of previous higher frequency surveys by two orders of magnitude. These initial results suggest that new low frequency telescopes, such as LOFAR, should detect many compact radio sources and that plans to extend these arrays to baselines of several thousand kilometres are warranted.

*Subject headings:* galaxies: active – quasars: individual (B0218+357, J0226+3421)  
– techniques: interferometry – radiation mechanisms: general

## 1. Introduction

The general properties of the 90 cm sky are not very well known and even less is known at VLBI resolution. Previous snapshot surveys at these wavelengths have only targeted the brightest sources and were plagued by poor sensitivity, radio interference and limited coherence times. Furthermore, the field of view that could be imaged was typically limited by the poor spectral and temporal resolution of early generation hardware correlators and the available data storage and computing performance at the time. As a result, although several hundred 90 cm VLBI observations have been made over the past two decades, images of only a few tens of sources have been published e.g. Altschuler et al. (1995); Joseph, Lazio, & Cordes (1998); Chuprikov et al. (1999); Cai et al. (2002). With such a small sample it is difficult to quantify the total population and nature of these sources. In particular, the sub-arcsecond and sub-Jansky population of 90 cm sources is largely unexplored.

Recent improvements to the EVN hardware correlator at JIVE (van Langevelde et al. 2004), have enabled significantly finer temporal and spectral resolution. Combined with vast improvements in storage and computing facilities, it is now possible to image fields as wide as, or even wider than, the FWHM of the primary beam of the observing instrument.

To complement the hardware improvements, new approaches to calibration and imaging have been developed to better utilise the available data and processing platforms. For example, Garrett, Wrobel & Morganti (2005) performed a deep VLBI survey at 20 cm of a 36′ wide field by using a central bright source as an in-beam calibrator. The approach was ideal for survey work as it permitted the imaging of many potential target sources simultaneously by taking advantage of the full sensitivity of the observation across the entire field of view. We have applied a similar technique at 90 cm by piggybacking on an existing VLBI observation of the gravitational lens B0218+357 and the nearby quasar J0226+3421, with the aim of surveying a 28 deg<sup>2</sup> field around each of the sources. The results provide an important indication of what may be seen by future low-frequency instruments such as the Low Frequency Array (LOFAR), European LOFAR (E-LOFAR) and the Square Kilometre Array (SKA).

In this paper, we present the results of a 90 cm wide-field VLBI survey that covers two partially overlapping regions of 28 deg<sup>2</sup> each, surveying 618 radio source targets at angular resolutions ranging between 30 and 300 mas. For sources located at a redshift of  $z = 1$ , the linear resolution corresponding to 30 mas is 230 pc. A *WMAP* cosmology (Spergel et al. 2003) with a flat Universe,  $H_0 = 72 \text{ km s}^{-1} \text{ Mpc}^{-1}$  and  $\Omega_m = 0.29$  is assumed throughout this paper.

## 2. Observations and Correlation

A VLBI observation of the gravitational lens B0218+357 was made on 11 November 2005 using all ten NRAO Very Long Baseline Array (VLBA) antennas, the Westerbork Synthesis Radio Telescope (WSRT) as a phased array and the Jodrell Bank, 76–m Lovell Telescope (JB). The primary aim of this observation was to investigate, in detail, propagation effects in the lensing galaxy and the substructure in the lens. The secondary aim, as investigated in this paper, was to serve as a wide-field test observation to study the faint source population at 90 cm over a good fraction of the primary beam.

The observation spanned 14 hours with approximately 6 hours of data recorded at JB and WSRT and 13 hours at the VLBA stations. Ten minutes scans of the target source B0218+357 ( $\alpha = 02^{\text{h}}21^{\text{m}}05^{\text{s}}.4733$  and  $\delta = 35^{\circ}56'13''.791$ ) were interleaved with three minute scans of the nearby quasar J0226+3421 ( $\alpha = 02^{\text{h}}26^{\text{m}}10^{\text{s}}.3332$  and  $\delta = 34^{\circ}21'30''.286$ ). Five minute scans of the fringe finder 3C84 were made approximately every four hours. Dual circular and cross polarisation data were recorded across four 4 MHz IFs centred on 322.49, 326.49, 330.49 and 610.99 MHz respectively, resulting in a total data recording rate of 128 Mbits s<sup>−1</sup>. The 610.99 MHz data were only recorded at the VLBA antennas. The data were

correlated at the European VLBI Network (EVN) correlator at the Joint Institute for VLBI in Europe (JIVE, Dwingeloo, the Netherlands) in multiple passes to create a single-IF, single polarisation, wide-field data set and a multi-IF, dual circular polarisation, narrow-field data set. The narrow-field data set concentrated on the B0218+357 with greater sensitivity and the results of this observation will be presented elsewhere (Wucknitz et al., in preparation). The wide-field data consisted of a single polarisation (LL), single IF with a 4 MHz band centred on 322.49 MHz. A third correlator pass centred on another source was used to create a second wide-field data set with a single IF and RR polarisation but was not used in our data reduction process.

To reduce the effects of bandwidth smearing and time averaging smearing, and thus image the largest possible field, the EVN correlator generated data with 512 spectral points per baseline and an integration time of 0.25 s. The spectral and temporal resolution exercised the current physical limits of the JIVE hardware correlator and resulted in a final data set size of 77.5 Gbytes. The wide-field data set has a one sigma theoretical thermal noise of  $\sim 1.2$  and  $\sim 0.7$  mJy/beam for the quasar and gravitational lens, respectively.

### 3. VLBI Calibration and Imaging

The data from the narrow-field data set were used to perform the initial editing and calibration of the phase reference to take advantage of the increased sensitivity available with the additional bands and polarisations. Nominal corrections to counter the effects of the total electron content (TEC) of the ionosphere were applied with the AIPS<sup>1</sup> task TECOR. An amplitude calibration table was derived from measures of the system temperature of each antenna throughout the observation using the AIPS task APCAL, and applied to the data set.

Delays across the IF bands, which were assumed to be constant throughout the observation, were calibrated by fringe fitting on 3C84. A multi-band fringe fit was then performed on the quasar. The flagging and calibration tables of the narrow-field data set were transferred to the wide-field data set using a ParselTongue<sup>2</sup> script. Further editing was applied to

---

<sup>1</sup>The Astronomical Image Processing System (AIPS) was developed and is maintained by the National Radio Astronomy Observatory, which is operated by Associated Universities, Inc., under co-operative agreement with the National Science Foundation

<sup>2</sup>A Python scripting tool for AIPS. ParselTongue was developed in the context of the ALBUS project, which has benefited from research funding from the European Community's sixth Framework Programme under RadioNet R113CT 2003 5058187. ParselTongue is available for download at

the wide-field data set to remove the frequency band edges and frequency channels adversely affected by RFI. The bandpass for the observation was calibrated against observations of 3C84.

As both the phase reference and the gravitational lens were to be used as in-beam calibrators for their respective fields, accurate calibration of the amplitudes and phases of both fields was essential. The calibration was complicated by the complex structure of both sources. To account for this structure a new DIFMAP (Shepherd, Pearson and Taylor 1994) task, *cordump*<sup>3</sup> (Lenc et al. 2006), was developed to enable the transfer of all phase and amplitude corrections made in DIFMAP during the imaging process to an AIPS compatible SN table. The *cordump* task greatly simplified the calibration of both of the fields. First, the phase reference data were averaged in frequency and exported to DIFMAP where several iterations of modelling and self-calibration of both phases and amplitudes were performed. *cordump* was then used to transfer the resulting phase and amplitude corrections back to the unaveraged AIPS data set. After application of these corrections, the DIFMAP model of the phase reference source was subtracted from the AIPS (u-v) data set. The quasar self-calibration solutions were then applied to the lens field as an initial calibration for that field. The calibration for the lens field was further refined using the same approach as for the quasar and upon completion the DIFMAP model of the lens was subtracted from the calibrated field. The images of the phase reference and the lens had measured RMS noise of 1.8 and 1.0 mJy beam<sup>-1</sup>, respectively. The higher than theoretical noise is attributed to substantial levels of RFI observed on some baselines and the shorter time available with the WSRT and JB observations.

In the first phase of the imaging process, the AIPS task IMAGR was used to make naturally weighted dirty images and beams of regions selected from WENSS data (Rengelink et al. 1997) of the two fields being surveyed, the source selection criteria are described in detail in § 4. Targets falling within a certain annulus around each field were imaged simultaneously using the multi-field option within IMAGR, the DO3D option was used to reduce non-coplanar array distortion. The data from both fields were kept in an unaveraged form to prevent smearing effects during imaging. For each target, the dirty image subtended a square of approximately 51'' on each side, an area that covers approximately half that of the WENSS beam at the observation declination (54'' × 92''). Since the dirty image of each target source contains  $\sim 2 \times 10^5$  synthesized-beam areas, a conservative 6 $\sigma$  detection threshold was imposed to avoid spurious detections. Furthermore, only the inner 75% of each dirty

---

<http://www.radionet-eu.org/rnwiki/ParselTongue>

<sup>3</sup>The *cordump* patch is available for DIFMAP at [http://astronomy.swin.edu.au/~sim\\$elenc/DifmapPatches/](http://astronomy.swin.edu.au/~sim$elenc/DifmapPatches/)

image was searched for candidate detections to avoid erroneous detections as a result of map edge effects. For each positive detection the coordinate of the VLBI peak flux density was recorded. This first imaging step was used to determine whether the target source had been detected with the VLBI observation. Based on our detection criteria, we estimate a false detection rate of approximately one in every 3300 images. While we expect the majority of unresolved WENSS sources to have peaks that fall within the imaged areas, approximately 9.5% of the WENSS sources exhibit resolved structure. For these sources, we would not detect bright compact components that may exist outside of the central region that was imaged.

During the calibration process, it was noted that the lens had significantly weaker signal on the longer baselines compared to that of the quasar. To test the effectiveness of the refined lens field self-calibration solutions, we re-imaged one of the B0218+357 field sources, B0215.1+3710, with only the phase reference self-calibration solutions applied. B0215.1+3710 is located on the side of the lens field that is furthest from the phase reference ( $\sim 3.45^\circ$ ) and so is most sensitive to changes from the nominal conditions that were corrected for. The target-calibrated dirty image for this source has an rms noise of  $4.7 \text{ mJy beam}^{-1}$  and a peak of  $42 \text{ mJy beam}^{-1}$ . With only the phase reference self-calibration solutions applied, the rms noise is  $6.6 \text{ mJy beam}^{-1}$  and the peak  $21 \text{ mJy beam}^{-1}$ . It is clear that without the refined calibration, B0215.1+3710 would not have been detected above the  $6\sigma$  threshold.

The second phase of the imaging process involved creating a (u,v) shifted data set for each of the positive detections, using the AIPS task UVFIX, such that the new image centre coincided with the coordinate of the image peak recorded in the first phase. The shifted data sets were averaged in frequency, effectively reducing the field of view of each of the targeted sources to approximately  $0.5'$ , and then exported to DIFMAP. In DIFMAP, the visibilities were averaged over 10 second intervals to reduce the size of the data set and to speed up the imaging process. Each target was imaged in DIFMAP, with natural weighting applied, using several iterations of model fitting. Phase self-calibration was performed between iterations to adjust for the varying effects of the ionosphere across the field.

During the imaging process it was noted that the self-calibration phase corrections varied significantly between fields and even among sources within each field. It is believed that these were due to ionospheric variations that occurred across the survey field. Observations at 90 cm will invariably suffer degradation as a result of ionospheric variations and the nominal TEC corrections made in the initial calibration stages assumed that these corrections would be valid across the entire field. This is not a valid assumption when imaging extremely large fields. To provide position dependent corrections within a field, ParselTongue scripts were

developed to implement two alternate methods that could be tested against the data.

The first method calculated ionospheric corrections based on TEC measures to each source of interest in the field of view and applied differential corrections, based on the TEC correction already made at the phase centre, prior to imaging. This allowed a differential correction to be applied after self calibrating on the bright central sources in each field of view of these observations. The corrections did not result in any significant improvement in the resulting images. We suspect that the currently available TEC solutions may be too coarse, both spatially and temporally, to account for the ionospheric variations across the field.

The second method used a parameterized ionospheric model to determine the corrections to each source of interest in the field of view. As with the TEC corrections, these were applied after the central source in each field had been self calibrated. Preliminary tests of these corrections indicated that they performed better than the differential TEC solutions with improvements of the order of a few percent in flux density observed in approximately 70% of sources tested.

The testing of these libraries is not yet complete and only the 11 wide-field sources of Lenc et al. (2006) were used in our initial tests. Further tests will be required to more robustly analyse the performance of the two approaches to ionospheric calibration.

Following our first attempt to survey the inner  $0^\circ - 1^\circ$  region of each field (Lenc et al. 2006) we discovered that the positional accuracy of the detected sources degraded significantly with radial distance from the phase centre when compared to the positions derived from observations with other instruments. While most sources observed with other instruments only had a positional accuracy of  $\sim 1''$  it was still clear that our fields were being scaled by a factor of  $0.99871 \pm 7 \times 10^{-5}$ , a factor that corresponds to an offset of  $53 \pm 3$  frequency channels in our data set. Interestingly, this appeared to corresponded to the 50 lower-band channels that were flagged during editing in the 31DEC05 version of AIPS that was used for the processing of the data. When the processing was repeated in the 31DEC06 version of AIPS, the positional discrepancies disappeared so we suspected that there may have been a software issue with the earlier version of AIPS. However, as wider fields were imaged we discovered four sources that were common to both of the fields. Each of these sources should have been well aligned between the two fields, however, discrepancies of  $0.41'' - 0.65''$  were being observed in approximately the same position angle. This was also indicative of a radial scaling but to a lesser degree,  $0.999927 \pm 1.4 \times 10^{-5}$ , corresponding to an offset of  $3 \pm 0.6$  channels. The source of this error has not yet been identified, however all of the sources positions and images in this paper have been corrected to account for this effect.

#### 4. Survey annuli, survey depths, and source selection

We split the survey of each field into six annuli based on the radial distance from the correlation phase centre of that field. These are referred to as the  $0^\circ - 0.25^\circ$ ,  $0.25^\circ - 0.5^\circ$ ,  $0.5^\circ - 1^\circ$ ,  $1^\circ - 1.5^\circ$ ,  $1.5^\circ - 2^\circ$ , and  $2^\circ - 3^\circ$  annuli in field 1 (centred on J0226+3421) and field 2 (centred on B0218+357). Our survey attempts to detect sources at large radial distances from the antenna pointing position and the correlation phase centre. To reduce the effect of bandwidth and time-averaging smearing, increasingly restrictive (u,v) ranges are employed in the outer annuli. Furthermore, the fall-off of the response of the primary beam is an effect that significantly limits the sensitivity within each annulus. In particular, WSRT and JB have significantly narrower primary beams ( $\sim 1'$  and  $\sim 0.5^\circ$  HWHM respectively), owing to their larger effective aperture, compared to the VLBA ( $\sim 1.3^\circ$  HWHM). As such, the WSRT data were only used to image the source directly at the phase centre, whilst the JB observatory data was only used in the  $0^\circ - 0.25^\circ$  annulus (restrictions in (u,v) range effectively excludes the JB data from the  $0.25^\circ - 0.5^\circ$  annulus even though it has a significant response within this annulus).

Since only the VLBA antennas were used outside the  $0^\circ - 0.25^\circ$  annulus, the reduced response in the other annuli is composed of only three independent components: the VLBA primary beam response ( $R_{VLBA}$ ) and the reduced response due to bandwidth and time-averaging smearing ( $R_{bw}$ ,  $R_t$ ). The combined reduced response,  $R$ , is given by  $R = R_{bw}R_tR_{VLBA}$ . We have estimated  $R_{bw}$  and  $R_t$  following Bridle & Schwab (1999) and have adopted a fitted function used to model the VLA antennas, as documented in the AIPS task PBCOR, to model the primary beam response of the VLBA under the assumption that the 25 m antennas in these arrays have a similar response (Garrett, Wrobel & Morganti 2005). In Table 1, we calculate the total response and estimated  $1\sigma$  rms noise at the outer edge of each annulus of the two surveyed fields. The (u,v) range has been restricted to limit the effects of bandwidth and time-averaging smearing to at most a few percent.

The WENSS catalogue was used as a guide for potential targets in the survey. Table 1 lists the total number of WENSS sources that exist within each annulus of each field. For a WENSS source to be detected by our survey it must have a peak flux density,  $S_P(\text{WENSS})$ , that satisfies the constraint  $S_P(\text{WENSS}) > 6\sigma R^{-1}$ . Estimates of this limit at the edge of each annulus,  $S_P$ , and the number of WENSS sources that meet this constraint,  $\langle N_{VLBI} \rangle$ , are listed in Table 1. Even though it was estimated that many of the WENSS sources would fall below our detection limits, for completeness, we targeted all WENSS sources in the  $0^\circ - 2^\circ$  annuli of each field given the possibility that some sources might exhibit strong variability. Between  $2^\circ - 3^\circ$  only candidate sources that were within our sensitivity limits were targeted.



## 5. Results

A total of 618 WENSS sources were targeted by the 90 cm wide-field VLBI survey at radial distances of up to  $2.89^\circ$  from the phase centre of the survey fields. The complete survey of all WENSS sources within the inner  $0^\circ - 2^\circ$  annulus of each field did not detect any source that had peak flux below our sensitivity limit, or that was partially resolved in WENSS. The combined total area imaged around each of the targeted sources in these fields represents  $\sim 0.5\%$  of the area surveyed.

Of all of the WENSS sources targeted, a total of 272 sources, 95 in the J0226+3421 field (field 1) and 177 in the more sensitive B0218+357 field (field 2), would have peak flux densities above our VLBI detection limits, if unresolved by our VLBI observations. The WENSS characteristics of these sources (position, peak flux density per solid beam angle, integrated flux and where available, the WENSS/NVSS spectral index  $\alpha$  where  $S_\nu \propto \nu^\alpha$ ) are listed in Tables 3 and 4 for fields 1 and 2, respectively. Where the target source is also detected by the VLBI survey, the corrected source position (see § 3), VLBI peak flux density per solid beam angle and integrated flux are listed in the following row. The VLBI peak and integrated flux density have been corrected for the primary beam response but not for bandwidth and time-averaging smearing losses. Based on these losses and uncertainties in the amplitude calibration, we estimate the absolute flux density scales of the VLBI observations to be better than 10% in the inner  $0.5^\circ$  of each field and better than 20% elsewhere.

A total of 27 sources were detected and imaged by the survey, eight of these sources detected in the J0226+3421 field (field 1) and the remaining 19 detected in the more sensitive B0218+357 field (field 2). Nine of the sources were detected outside of the half-power point of the VLBA primary beam (HWHM  $\sim 1.3^\circ$ ). Four sources, B0223.1+3408, B0221.9+3417, B0219.2+3339 and B0223.5+3542, were detected in both fields in the region of overlap. B0219.2+3339, in particular, was detected at  $2.06^\circ$  from the phase centre of the second field and is well past the quarter power point of the VLBA primary beam, it is also the only source detected in the outer annulus of the survey. Table 2 lists all of the detected sources, the detection field, the distance from the phase centre of that field, the restoring beam size and the one sigma residual RMS noise. A positional comparison of our corrected source positions is also made with respect to the best known radio positions, where  $d_E$  and  $\theta_E$  are the observed offset and position angle from this position, and  $d_\sigma$  is the offset in terms of the combined one sigma position error of the two compared positions.

The VLBI positions in the  $0^\circ - 0.25^\circ$  and  $0.25^\circ - 0.5^\circ$  annuli are limited by errors introduced by the ionosphere. We estimate a one sigma error of  $\sim 3 - 12$  mas in each coordinate. The positional accuracy of the outer, heavily tapered, annuli are further limited by RMS noise errors. We estimate the one sigma error in each coordinate of these outer fields

to be better than 15 mas, 20 mas and 30 mas for the  $0.5^\circ - 1^\circ$ ,  $1^\circ - 1.5^\circ$  and  $1.5^\circ - 2^\circ$  annuli, respectively. The positional accuracy of B0219.2+3339 is also expected to be  $\sim 30$  mas as it is located quite close to the  $2^\circ$  boundary. After a correction was applied for an apparent scaling effect in the image (see § 3), residual errors of 40 mas, 100 mas, 200 mas and 180 mas were measured for the cross-field detections of sources B0223.1+3408, B0221.9+3417, B0219.2+3339 and B0223.5+3542 respectively. These extremely wide-field sources exhibited significant ionospheric phase fluctuations that distorted their initial dirty images. While the fluctuations were partially corrected for with phase self-calibration, it is believed that this may have adversely affected the position accuracy.

Contour maps for each of the sources detected in field 1 are shown in Figure 2 and those detected in field 2 are shown in Figure 3. While not formally part of the wide-field survey, the fringe finder 3C84 has also been imaged and is shown in Figure 4.

The total survey required nearly six weeks of processing on a single 2 GHz computer, required  $\sim 200$  gigabytes of workspace, and generated a total of  $\sim 20$  gigabytes of image data. We estimate that six years of processing would be required to completely image the FWHM beam of the VLBA at 320 MHz using similar techniques. Fortunately, the problem can be easily broken down to run efficiently in the parallel environment of a supercomputing cluster. With a basic 100-node cluster, the entire FWHM beam of the VLBA could be imaged within three weeks using a simple brute force method that would image targets on individual processors. For a single field, the cluster would generate mosaic of the primary beam comprising of  $\sim 1$  terabyte of image data. More elaborate algorithms may be employed to improve the efficiency of this processing further, for example, by using a recursive approach that creates successively smaller sub-fields by performing a combination of (u-v) shifting and data averaging.

## 5.1. Comments on individual sources

### 5.1.1. 3C84

For 3C84, we measure a VLBI peak flux density of  $2.33 \text{ Jy beam}^{-1}$  and an integrated flux of 6.07 Jy, whereas the WENSS peak flux density and integrated flux is  $19.396 \text{ Jy beam}^{-1}$  and 42.8 Jy respectively. This is the only source in our sample of imaged sources with extended structure in WENSS, where it has an estimated size of  $115'' \times 84''$  at a position angle of  $115^\circ$ . In our VLBI image we have recovered  $\sim 14\%$  of the WENSS flux. Similar VLBI observations at 327 MHz, with a larger synthesised beam, measure a slightly greater integrated flux of 7.47 Jy (Ananthakrishnan et al. 1989) suggesting that the missing flux is

most likely related to the larger-scale structure that is resolved out by VLBI observations. We measure a Largest Angular Size (LAS) of 150 mas which corresponds to a Largest Linear Size (LLS) of  $\sim 50$  pc at its measured redshift of  $z = 0.017559 \pm 0.000037$  (Strauss et al. 1992). A 15 GHz VLBA contour map (Lister, & Homan 2005) is shown overlaid with our 90 cm image of 3C84 in Figure 4. The smaller scale structures within this image appear to align with the jet-like feature that appears in our 90 cm image and extends 100 mas to the south of the core.

### 5.1.2. *B0223.1+3408 (J0226+3421, 4C+34.07)*

The quasar, J0226+3421, was imaged with the full (u,v) range and recovers approximately 80% of the WENSS flux. The contour map of this source is shown in Figure 2(a) and is overlaid with a naturally weighted 2 cm A-configuration VLA with Pie Town contour map (Wucknitz et al., in preparation). The source is dominated by a bright core ( $\sim 0.85$  Jy) and an extended lobe to the west ( $\sim 1.6$  Jy). A weaker lobe appears to the north ( $\sim 0.28$  Jy) and a partially resolved hot spot ( $\sim 0.14$  Jy) approximately mid-way between the core and the western lobe. The source has a LAS of  $1.15''$  which corresponds to a LLS of  $\sim 9$  kpc at its measured redshift of  $z = 2.91 \pm 0.002$  (Willott et al. 1998). All of the large-scale structures observed at 90 cm with VLBI are also clearly detected at 2 cm with the VLA and Pie Town. MERLIN+VLBI images at 18 cm (Dallacasa et al. 1995) detect the core and western lobe with large-scale structure and positions that are consistent with our image, however, their observations do not detect the northern lobe or hot spot. The source was also detected in the second field and is shown in Figure 3(q) with an image of the field 1 source restored using the same beam. An offset of 40 mas is observed between the field 1 and field 2 source after correcting for the larger-scale offset described in § 3.

### 5.1.3. *B0218.0+3542 (B0218+357)*

B0218.0+3542 is a gravitational lens that has been mapped at higher frequencies (e.g. Biggs et al. 2001; Wucknitz et al. 2004), with VLBI (e.g. Biggs et al. 2003), and at various wavelengths by Mittal et al. (2006). The source is the smallest known Einstein radio ring (Patnaik et al. 1993). As this source was the main target of the original observation, it is placed in the most sensitive field and annulus of the survey and has been imaged with the full (u,v) range. Our image of the source, Figure 3(a), has been restored with a beam that is  $\sim 4$  times larger than normal to highlight the large-scale structure within the source. The source has a LAS of 690 mas and is dominated by the A and B lensed images to the west and

east, respectively. The two images are separated by  $\sim 340$  mas and appear to have weaker components that are mirrored on either side of the lens. These weaker components may be a small portion of a lensed jet that is tangentially stretched. Our observations recover  $\sim 54\%$  of the WENSS flux suggesting the presence of structures that are fully resolved out even with our shortest baselines. L-Band VLA images of the source seem to suggest that there is indeed a larger-scale emission surrounding the source (O’Dea et al. 1992). The measured redshift of the lensing galaxy  $z = 0.68466 \pm 0.00004$  (Browne et al. 1993) and that of the lensed object is  $z = 0.944 \pm 0.002$  (Cohen, Lawrence & Blandford 2003). B0218.0+3542 will be studied in greater detail with the high sensitivity, narrow-field observations of this source at 327 MHz and at 610 MHz by Wucknitz et al. (in preparation).

#### 5.1.4. *B0221.9+3417*

The VLBI source we detect within the B0221.9+3417 field, Figure 2(b), is offset by  $9.94''$  and at a position angle of  $146^\circ$  compared to the WENSS position. The source is also detected in field 2, Figure 3(o). The separation between both detections is within 100 mas, after correcting for the larger-scale offset described in § 3, and both have a similar flux density confirming that the detected source is indeed at this position. The position offset also exists when compared against the same source in NVSS, the 365 MHz Texas survey (Douglas et al. 1996) and VLSS (Cohen et al. 2006). As only 11% of the WENSS flux was recovered by the VLBI observation, the position offset hints at a larger component  $\sim 10''$  to the north-west of the VLBI source. Furthermore, NVSS lists a fitted source size with a major axis of  $16''$  and the Texas survey categorises the source as a symmetric double with a component separation of  $13 \pm 2''$  at a position angle of  $155 \pm 11^\circ$ . These observations are consistent with the VLBI observation if we assume a compact south-eastern component has been detected. The VLBI source has a weaker component 360 mas to the north-west that is directly in line with the WENSS source. We measure a LAS of 360 mas for the VLBI source and an LLS 2.8 kpc at its measured redshift of  $0.852 \pm 0.002$  (Willott et al. 2002).

#### 5.1.5. *B0221.6+3406B*

B0221.6+3406B, as shown in Figure 2(c), has a complex morphology. The source has an LAS of 830 mas which corresponds to a LLS of 6.7 kpc at a measured redshift of  $z = 2.195 \pm 0.003$  (Willott et al. 1998). Our VLBI observations have recovered  $\sim 90\%$  of the WENSS flux suggesting that there is little or no extended structure above what has already been imaged. Based on the integrated flux densities in WENSS and NVSS, the source has a

spectral index of  $-0.93$ .

#### 5.1.6. *B0223.9+3351*

B0223.9+3351, as shown in Figure 2(d), appears to be an AGN with a 180 mas jet extension to the north. The source has a LAS of 420 mas which corresponds to a LLS of 3.5 kpc at a measured redshift of  $z = 1.245 \pm 0.004$  (Willott et al. 2002). Our VLBI observations have recovered  $\sim 50\%$  of the WENSS flux.

#### 5.1.7. *B0215.4+3536*

B0215.4+3536 is an ultra-steep spectrum source, a characteristic that is an excellent tracer of galaxies at redshifts  $z \geq 2$  (e.g. Röttgering et al. 1994, and references therein). The source has a LAS of  $7.1''$  which corresponds to a LLS of  $\geq 60$  kpc for a redshift of  $z \geq 2$ . Figure 3(e) shows our 90 cm VLBI image overlaid with an L-Band VLA image (Röttgering et al. 1994). The core and peaks within the two lobes align very closely, to within  $0.1\sigma$ , with the VLA image. A compact component of emission, possibly a jet interaction region, is detected by our observations approximately mid-way between the core and the south-west lobe and appears to align with extended edge of that lobe. Approximately 50% of the WENSS flux is recovered by our observation, the remaining flux is likely associated with the extended lobes and is resolved out by our observation.

#### 5.1.8. *B0219.2+3339*

B0219.2+3339 is detected in both field 1 and field 2 and is shown in Figures 2(g) and 3(s), respectively. A significant residual offset of 200 mas exists between these two independent detections even after correcting for the larger-scale offset described in § 3. The phases of this source in the J0226+3421 field appeared to be more heavily affected by the ionosphere than those in the B0218+357 field and it is believed that the offset may have been introduced by the phase self-calibration process. The source has a LAS of 900 mas which corresponds to a LLS of 6.6 kpc for a measured redshift of  $z = 0.752 \pm 0.002$  (Willott et al. 2002).

### 5.1.9. *B0214.5+3503*

B0215.4+3503 has been previously imaged by Röttgering et al. (1994) at L-Band with the VLA and is classified as an ultra-steep spectrum source. Contours of the L-Band VLA image are shown overlaid with the 90 cm VLBI observation in Figure 3(h). The source has a LAS of  $2.8''$  which corresponds to a LLS of  $\geq 24$  kpc if a redshift of  $z \geq 2$  is assumed. The two components of the VLBI source align very closely, to within  $0.2\sigma$ , with the VLA image. Approximately 75% of the WENSS flux is recovered by our observation, the remaining flux is likely associated with the extended structure observed in the VLA image.

### 5.1.10. *B0223.5+3542*

B0223.5+3542 is detected in both field 1 and field 2 and is shown in Figures 2(h) and 3(j), respectively. A significant residual offset of 180 mas exists between these two independent detections even after correcting for the larger-scale offset described in § 3. The phases of the source in the J0226+3421 field appeared to be more heavily affected by the ionosphere than those in the B0218+357 field and it is believed that the offset may have been introduced by the phase self-calibration process. This may have also adversely affected the measure of the integrated flux density which is approximately 60% greater in the J0226+3421 field compared to the B0218+357 field. The two components of the source are separated by 830 mas. Approximately 90% of the WENSS flux is recovered in the B0218+357 field observation of this source.

### 5.1.11. *B0223.8+3533*

Observations of this field revealed an unresolved compact source, Figure 3(k), approximately  $17''$  from the position reported by WENSS and over  $25''$  from the more accurate position reported by NVSS, these are by far the greatest offsets observed in all of our detected sources. NVSS also places a limit on the fitted major axis of this source at less than  $15''$ , a size that does not encompass our observed source. Furthermore, our measure of integrated flux of 90 mJy is more than twice that measured by WENSS. The size, position and integrated flux density of our VLBI source suggest that it may be an unrelated transient or highly variable source that has been serendipitously detected within the target field. The existence of this source was tested by splitting the VLBI data into four equal length periods and independently imaging each of these. The source was detected in all four data sets with an integrated flux of  $92 \pm 11$  mJy beam $^{-1}$ . Furthermore, as would be expected for an unre-

solved source, scalar averaging of the visibility amplitudes over 30 minute intervals revealed amplitudes that were approximately equal on all baselines.

#### 5.1.12. *B0211.9+3452*

We observe an almost  $7''$  offset at a position angle of  $13^\circ$  between our VLBI detection of this source, Figure 3(1), and the best known position (Condon et al. 1998). NVSS places a limit on the fitted HWHM model of this source at less than  $28.6''$  and also notes the presence of large residual errors which are indicative of a complex source. As only 30% of the WENSS flux was recovered by the VLBI observation there is a suggestion that we have detected a compact component of a larger source. This is also supported by the 365 MHz Texas survey which classifies the source as an asymmetric double with a separation of  $27 \pm 1''$  at a position angle of  $25 \pm 2^\circ$ .

## 6. Discussion

Our survey results indicate that at least 10% of moderately faint ( $S \sim 100$  mJy) sources found at 90 cm contain compact components smaller than  $\sim 0.1$  to  $0.3$  arcsec and stronger than 10% of their total flux densities. This is a strict lower limit as the sensitivity of our observation was limited by the primary beam at the edge of the survey fields. None of the surveyed sources that were even slightly resolved by WENSS were detected. Similarly, none of the WENSS sources that were below the sensitivity limits of the VLBI observation were detected either, suggesting that none of these sources had significantly increased in brightness since the WENSS observations were carried out.

The apparent lack of sources varying above our detection threshold must at least in part be due to resolution effects. As 90% of the WENSS sources above the VLBI detection threshold are not detected they must be at least partially resolved at the VLBI resolution and the compact component of the radio emission would only be a fraction of the WENSS flux density. For the compact component of these sources to vary enough to be detected with VLBI, they must increase in strength by factors of perhaps at least a few (the reciprocal of the ratio of compact flux to WENSS flux) to be detectable with VLBI; the compact component of the flux needs to increase above the VLBI sensitivity limit. Resolution effects are masking variability in these sources. As discussed below, the detection of one apparent highly variable source in the VLBI data is rather remarkable.

The interpretation of our detection statistics is complicated, in that the survey has a

non-uniform sensitivity over both fields, due to the primary beam response of the VLBA antennas and the fact that we are imaging objects well beyond the half-power points of the primary beam. In addition, due to time and bandwidth smearing effects, as one images objects further from the phase centre, data on the long baselines is discarded, since the smearing effects make imaging difficult. A consequence of this is that the angular resolution is also non-uniform across the surveyed fields, with low resolution far from the phase centre. Not only is the flux limit variable across the field, the brightness temperature sensitivity also varies.

It is possible to estimate the detection statistics of our survey for a uniform flux density and brightness temperature limit by considering sources not too far from the phase centre and for a flux sensitivity between the extremes at the phase centre and field edge. For example, if a sensitivity limit of  $30 \text{ mJy beam}^{-1}$  is considered (achieved in the  $0.25 - 0.5$  degree annulus of field 1 and in the  $0.5 - 1$  degree annulus of field 2, and exceeded in the lower radius annuli in each field), 11 out of 55 possible sources are detected, a detection rate of 20%, higher than the strict lower limit of 10% estimated above for all sources at all annuli.

Garrett, Wrobel & Morganti (2005) performed a similar survey of the NOAO Bootes field at 1.4 GHz, using the NRAO VLBA and 100 m Green Bank Telescope. The survey covered a total of  $0.28 \text{ deg}^2$ , one hundredth of the area covered by our survey, and detected a total of 9 sources. The survey achieved sensitivities of  $0.074 - 1.2 \text{ mJy beam}^{-1}$  that enabled the detection of both weak and extended sources, whereas our 90 cm observations detected mainly compact sources or slightly resolved bright sources. Nonetheless, we can estimate the number of detections in this region that could be achieved using the 90 cm survey techniques described in this paper. The  $0.28 \text{ deg}^2$  NOAO Bootes field contains a total of 13 WENSS sources, 6 of which have integrated flux densities  $> 30 \text{ mJy}$ . Based on our detection rate of 20% for such sources we would expect to detect one WENSS source at 90 cm. Assuming a median spectral index of  $-0.77$ , only two of the Garrett, Wrobel & Morganti (2005) sources have integrated flux densities above our  $30 \text{ mJy beam}^{-1}$  limit at 90 cm, however, one of these is extended and would have a VLBI peak flux density that falls below our limit. Thus the observations of Garrett, Wrobel & Morganti (2005) are consistent with our 90 cm VLBI results for sources with a peak flux density above  $30 \text{ mJy beam}^{-1}$ .

Estimates of the percentage of sources detected with VLBI gives an estimate of the relative contribution of AGN (that contain compact radio emission and are detectable with VLBI) and starburst galaxies (which contain low brightness temperature radio emission not detectable with VLBI). Analysis of the ratio of starburst galaxies to AGN as a function of redshift (at high redshifts) can help to determine the initial sources of ionising radiation early in the Universe. As very little redshift data for our surveyed sources are available,



such an analysis is not currently possible with this dataset. In practice, VLBI data at an additional frequency is also required, to confirm that the compact radio emission attributed to AGN has plausible spectral indices.

The distribution of morphologies in the detected survey sources are typical of AGN. 10/27 sources are unresolved point sources, consistent with core-dominated AGN. A further 8/27 are clearly resolved into double component sources, consistent with being core-jet AGN or double-lobed radio galaxies. 7/27 sources have complex or extended structures, not obviously clear double components. Again, these sources may be core-jet AGN or radio galaxies. The remaining 2/27 sources are the gravitational lens and the quasar at the phase centres of the two fields.

The serendipitous detection of a likely highly variable, very compact source near the target WENSS source B0223.8+3533 is intriguing. The total area imaged by this survey represents  $\sim 0.5\%$  of the area within the  $0^\circ - 2^\circ$  annulus and is equivalent to  $\sim 2.2\%$  of the FWHM of the VLBA primary beam. While it is difficult to place any limits on the real population of variable sources based on this one observation, it does highlight the importance of imaging wide-fields completely, in order to improve our understanding of such sources.

## 6.1. Future Prospects

The observations presented here demonstrate that extremely wide-field surveys can now be piggybacked on current and future VLBI observations at 90 cm. While this survey has mainly concentrated on detecting and imaging sources already detected by other surveys, we find tantalising evidence of a transient or highly variable source. We were fortunate to have found one that appeared in close proximity to one of our target sources but this may not always be the case. This provides a motive to take on a more ambitious survey of the entire field. Such a survey is not beyond the reach of current technology, it would require at most  $\sim 45$  times more processing compared to the project presented here, in order to image the entire primary beam of the VLBA using a similar faceted approach. While this is not the most efficient means of detecting transients, it will help progress the development of algorithms and techniques needed for next generation, survey-class instruments that operate at wavelengths or sensitivities not matched by current instruments.

The observations presented in this paper were limited by the spectral and temporal resolution of the EVN correlator at the time of the observation. To minimise the effects of bandwidth and time-averaging smearing it was necessary to compromise resolution and image noise. Future technical developments in the capabilities of correlators will allow wide-

field, global VLBI studies to be conducted without such restrictions. In particular, software correlators can provide extremely high temporal and spectral resolution, limited only by the time it takes to process the data (Deller et al. 2007). They also allow for some pre-processing to be applied during the correlation process to, for example, mitigate the effects of radio interference or to correlate against multiple phase centres simultaneously.

## 6.2. Implications for LOFAR and SKA

The results of these observations provide important information on the nature and incidence of compact, low-frequency radio sources, with consequences for next generation, low-frequency instruments such as LOFAR and the SKA. LOFAR is currently being deployed across The Netherlands but remote stations are already under construction in neighbouring countries, in particular Germany. Other countries (e.g. UK, France, Sweden, Italy and Poland) are also expected to join this European expansion of LOFAR (E-LOFAR), extending the longest baseline from a few hundred, to a few thousand km. This development will provide LOFAR with sub-arcsecond resolution at its highest observing frequency (the 120 – 240 MHz high-band). One concern associated with extending LOFAR to much longer baselines is whether enough cosmic sources will remain unresolved - this characteristic is required in order to ensure there are enough calibrator sources in the sky in order to calibrate the instrument across its full, very wide, field-of-view. The observations presented here suggest that at least one tenth of all radio sources (at the several tens of mJy level) are likely to exhibit compact VLBI radio structure in the LOFAR high-band. In all likelihood, an even larger fraction of the E-LOFAR source population will therefore be bright and compact enough to form a grid of calibrator sources across the sky. From our results, we estimate the spatial number density of relatively bright ( $S > 10$  mJy) and compact ( $LAS < 200$  mas) sources at 240 MHz to be  $\sim 3 \text{ deg}^{-2}$ . The aggregate total of these compact sources within a beam should serve as a good calibrator for E-LOFAR and enable most of the low-frequency radio sky to be imaged with excellent sub-arcsecond resolution and high dynamic range. Extrapolation to LOFAR’s low-band (10–80 MHz) is probably very dangerous, but there is every reason to believe that a large number of these sources will remain compact.

In order to assess the relative numbers of starburst galaxies and AGN as a function of redshift, obviously large redshift surveys need to take place for these radio continuum objects. Such a survey could be conducted using the redshifted HI signal from these galaxies, using the SKA.

E.L. acknowledges support from a Swinburne University of Technology Chancellor’s

Research Scholarship, a CSIRO Postgraduate Student Research Scholarship, ATNF co-supervision, and the hospitality of JIVE where part of this work was carried out. This work was supported by the European Community’s Sixth Framework Marie Curie Research Training Network Programme, Contract No. MRTN-CT-2004-505183 “ANGLES”. This research has made use of the NASA/IPAC Extragalactic Database (NED), which is operated by the Jet Propulsion Laboratory, California Institute of Technology, under contract with the National Aeronautics and Space Administration. The National Radio Astronomy Observatory is a facility of the National Science Foundation operated under cooperative agreement by Associated Universities, Inc. The European VLBI Network is a joint facility of European, Chinese, South African and other radio astronomy institutes funded by their national research councils.

## REFERENCES

- Altschuler, D.R., Gurvits, L.I., Alef, W., Dennison, B., Graham, D., Trotter, A.S., Carson, J.E. 1995, *ApJS*, 114, 197
- Ananthakrishnan, S., et al. 1989, *MNRAS*, 237, 341
- Beasley, A.J., Gordon, D., Peck, A.B., Petrov, L., MacMillan, D.S., Fomalont, E.B., & Ma, C. 2002, *ApJS*, 141, 13
- Biggs, A.D., Browne, I.W.A, Muxlow, T.W.B., & Wilkinson, P.N. 2001, *MNRAS*, 322, 821
- Biggs, A.D., Wucknitz, O., Porcas, R.W., Browne, I.W.A., Jackson, N.J., Mao, S., & Wilkinson, P.N. 2003, *MNRAS*, 338, 599
- Bridle, A.H., & Schwab, F.R. 1999, in *ASP Conf. Ser. 180, Synthesis Imaging in Radio Astronomy II*, ed. G.B. Taylor, C.L. Carilli, & R.A. Perley (San Francisco: ASP), 371
- Browne, I.W.A., Patnaik, A.R., Walsh, D. & Wilkinson P.N. 1993, *MNRAS*, 263, 32
- Cai, Z., et al. 2002, *A&A*, 381, 401
- Chuprikov, A.A., et al. 1999, *New A Rev.*, 43, 747
- Condon, J.J., Cotton, W.D., Greisen, E.W., Yin, Q.F., Perley, R.A., Taylor, G.B., & Broderick, J.J. 1998, *AJ*, 115, 1693
- Cohen, A.S., Lane, W.M., Cotton, W.D., Kassim, N.E., Lazio, T.J.W., Perley, R.A., Condon, J.J., Erickson, W.C. 2007, *AJ*, 134, 1245

- Cohen, J.G., Lawrence, C.R., & Blandford, R.D. 2003, *ApJ*, 583, 67
- Dallacasa, D., Fanti, C., Fanti, R., Schilizzi, R.T., & Spencer, R.E. 1995, *A&A*, 295, 27
- Deller, A.T.; Tingay, S.J.; Bailes, M.; West, C. 2007, *PASP*, 119, 318
- Douglas, J.N., Bash, F.N., Bozyan, F.A., Torrence, G.W., & Wolfe, C. 1996, *AJ*, 111, 1945
- Garrett, M.A., Wrobel, J.M., & Morganti, R. 2005, *ApJ*, 619, 105
- Hales, S.E.G., Baldwin, J.E., Warner, P.J. 1993, *MNRAS*, 263, 25
- Lazio, T.J.W., & Cordes, J.M. 1998, *ApJS*, 115, 225
- Lenc, E., Garrett, M.A., Wucknitz, O., Anderson, J.M., & Tingay, S.J. 2006, in *Procs. of the 8th EVN Symposium*, ed. W. Baan et al. (astro-ph/0612618)
- Lister, M.L., & Homan, D.C. 2005, *AJ*, 130, 1389
- Mittal, R., Porcas, R., Wucknitz, O., Biggs, A., & Browne, I. 2006, *A&A*, 447, 515
- O’Dea, C.P., Baum, S.A., Stanghellini, C., Dey, A., van Breugel, W., Deustua, S., & Smith, E.P. 1992, *AJ*, 104, 1320
- Patnaik, A.R., Browne, I.W.A., Wilkinson, P.N., & Wrobel, J.M. 1992, *MNRAS*, 254, 655
- Patnaik, A.R., Browne, I.W.A., King, L.J., Muxlow, T.W.B., Walsh, D., & Wilkinson, P.N. 1993, *MNRAS*, 261, 435
- Rengelink, R.B., Tang, Y., de Bruyn, A.G., Miley, G.K., Bremer, M.N., Röttgering, H.J.A., & Bremer, M.A.R. 1997, *A&AS*, 124, 259
- Röttgering, H.J.A., Lacy, M., Miley, G.K., Chambers, K.C., & Saunders, R. 1994, *A&AS*, 108, 79
- Shepherd, M.C., Pearson, T.J., & Taylor, G.B. 1994, *BAAS*, 26, 987
- Spergel, D.N., et al. 2003, *ApJS*, 148, 175
- Strauss, M.A., Huchra, J.P., Davis, M., Yahil, A., Fisher, K.B., & Tonry, J. 1992, *ApJS*, 83, 29
- van Langevelde, H.J., Verkouter, H., Parsley, S., Garrett, M., Olon, F., & Kramer, B. 2004, in *Procs. of the 7th EVN Symposium*, ed. R. Bachiller et al. (astro-ph/0412292)

- Willott, C.J., Rawlings, S., Blundell, K.M., & Lacy, M. 1998, MNRAS, 300, 625
- Willott, C.J., Rawlings, S., Blundell, K.M., Lacy, M., Hill, G.J. & Scott, S.E. 2002, MNRAS, 335, 1120
- Wucknitz, O., Biggs, A.D., & Browne, I.W.A 2004, MNRAS, 349, 14

Table 1. Survey Fields, Depths and Source Counts at 324 MHz.

Survey Field <sup>a</sup>	Annulus Range (arcdeg)	Maximum ( $u, v$ ) Range (M $\lambda$ )	Response R <sup>b</sup>	$1\sigma$ rms Noise <sup>b</sup> (mJy beam <sup>-1</sup> )	Survey Resolution (mas, mas)	$S_P$ <sup>b</sup> (mJy beam <sup>-1</sup> )	$N_{WENSS}$	$\langle N_{VLBI} \rangle$ <sup>c</sup>
1	0.00 – 0.25	2.50	0.94	3.7	40 × 20	> 24	4	3
1	0.25 – 0.50	1.00	0.89	4.8	140 × 130	> 32	15	10
1	0.50 – 1.00	0.75	0.65	6.8	180 × 170	> 63	55	27
1	1.00 – 1.50	0.75	0.36	8.9	230 × 220	> 147	91	28
1	1.50 – 2.00	0.50	0.17	11.0	350 × 290	> 378	128	16
1	2.00 – 3.00	0.50	0.06	15.1	360 × 290	> 1603	411	11
2	0.00 – 0.25	2.50	0.94	1.9	90 × 80	> 12	2	2
2	0.25 – 0.50	1.00	0.89	2.3	140 × 130	> 16	15	15
2	0.50 – 1.00	0.75	0.65	3.2	180 × 170	> 30	50	44
2	1.00 – 1.50	0.75	0.36	4.1	230 × 220	> 68	97	52
2	1.50 – 2.00	0.50	0.17	5.1	350 × 290	> 174	128	41
2	2.00 – 3.00	0.50	0.06	6.9	360 × 290	> 749	375	23

<sup>a</sup>Field 1 is centred about J0226+3421 and field 2 is centred about B0218+357.

<sup>b</sup>The estimated worst case values at the edge of the annulus.

<sup>c</sup>The number of WENSS sources that, if unresolved, have a peak flux that would fall above the estimated VLBI sensitivity limit.

Table 2. Source and image characteristics and astrometric errors.

WENSS Source	Source Location		Image Characteristics			Ref. <sup>d</sup>	Position Comparison		
	Field <sup>a</sup>	$d_{PC}$ <sup>b</sup> (arcdeg)	Beam Size (mas,mas)	Beam P.A. (degrees)	$1\sigma$ Noise <sup>c</sup> (mJy beam <sup>-1</sup> )		$d_E$ <sup>e</sup> (arcsec)	$\theta_E$ <sup>f</sup> (degrees)	$d_\sigma$ <sup>g</sup> ( $\sigma_p$ )
3C84	...	...	$31 \times 15$	-17	6.1	BE02	0.002	228	0.7
B0223.1+3408	1	0.00	$37 \times 19$	-13	1.8	BE02	0.002	270	0.7
...	2	1.89	$360 \times 285$	-42	5.8	BE02	0.042	125	1.4
B0218.0+3542	2	0.00	$64 \times 43$	52	1.0	PA92	0.024	75	0.9
B0219.1+3533	2	0.27	$88 \times 84$	80	1.5	CO98	0.173	168	0.1
B0221.9+3417	1	0.29	$145 \times 132$	38	4.4	DO96	9.938	34	13.2
...	2	1.63	$361 \times 285$	-42	4.1	DO96	10.003	34	13.0
B0221.6+3406B	1	0.31	$145 \times 132$	37	4.1	CO98	0.613	160	0.6
B0223.9+3351	1	0.32	$145 \times 132$	38	4.3	CO98	1.432	55	1.5
B0221.6+3406A	1	0.33	$145 \times 132$	37	4.3	CO98	1.178	42	0.8
B0216.6+3523	2	0.42	$142 \times 133$	31	2.2	CO98	0.437	188	0.4
B0220.1+3532	2	0.46	$142 \times 134$	30	2.0	CO98	0.215	313	0.2
B0215.4+3536	2	0.54	$180 \times 170$	23	2.5	RÖ94	0.103	56	0.1
B0223.2+3441	1	0.55	$180 \times 168$	38	5.0	CO98	1.382	317	1.1
B0220.7+3551	2	0.56	$180 \times 170$	23	2.4	CO98	0.231	148	0.2
B0215.8+3626	2	0.87	$227 \times 217$	-38	3.0	CO98	0.226	354	0.2
B0219.2+3339	1	0.93	$224 \times 218$	-62	6.3	CO98	0.572	46	0.6
...	2	2.06	$359 \times 284$	-43	4.2	CO98	0.374	42	0.4
B0214.5+3503	2	0.96	$227 \times 217$	-36	3.9	RÖ94	0.162	49	0.2
B0215.4+3636	2	1.04	$228 \times 217$	-36	3.3	CO98	0.579	114	0.6
B0223.5+3542	2	1.12	$228 \times 217$	-37	5.3	DO96	0.833	295	1.8
...	1	1.57	$357 \times 287$	-44	9.1	DO96	0.783	308	1.6
B0223.8+3533	2	1.19	$228 \times 217$	-35	3.1	CO98	25.146	344	11.0
B0211.9+3452	2	1.50	$227 \times 217$	-37	3.6	CO98	6.936	344	10.6
B0214.3+3700	2	1.51	$352 \times 286$	-40	4.6	CO98	2.544	271	2.6
B0215.1+3710	2	1.58	$353 \times 287$	-41	4.1	CO98	0.368	322	0.4
B0226.5+3618	2	1.81	$360 \times 288$	-40	3.8	CO98	1.362	192	1.4
B0225.1+3659	2	1.92	$358 \times 288$	-40	5.3	CO98	0.256	143	0.3

<sup>a</sup>Field 1 is centred about J0226+3421 and field 2 is centred about B0218+357.

<sup>b</sup>Distance of the source from the phase centre of the observed field.

<sup>c</sup>The  $1\sigma$  residual noise after the source model has been subtracted from the image.

<sup>d</sup>References for positions. BE02 = 2.3/8.3 GHz VLBA (Beasley et al. 2002); CO98 = 1.4 GHz VLA (Condon et al. 1998); DO96 = 365 MHz Texas interferometer (Douglas et al. 1996); PA92 = 8.4 GHz VLA (Patnaik et al. 1992); RÖ94 = 1.4 GHz VLA (Röttgering et al. 1994)

<sup>e</sup>The measured offset of the VLBI source peak from the position listed in reference.

<sup>f</sup>The position angle of the VLBI source peak in relation to the position listed in reference.

<sup>g</sup>The measured offset of the VLBI source peak in relation to the position listed in reference in terms of the  $1\sigma$  astrometric precision  $\sigma_p$ .

Table 3. Astrometry and Photometry at 324 MHz for field 1 targets.

Annulus	WENSS Source	R.A. (J2000.0)	Decl. (J2000.0)	$S_P$ (mJy beam <sup>-1</sup> )	$S_I$ (mJy)	$\alpha$
0° – 0.25°	B0223.1+3408	02 26 10.15	+34 21 30.7	3793	3678	−0.16
	...	02 26 10.3332	+34 21 30.286	375	2880	...
	B0222.2+3406	02 25 14.12	+34 20 22.4	32	33	−1.09
	B0222.3+3414	02 25 19.18	+34 27 31.7	41	50	...
0.25° – 0.5°	B0221.9+3417	02 24 56.18	+34 30 35.8	1657	1638	−0.91
	...	02 24 56.620	+34 30 27.47	111	186	...
	B0224.1+3354	02 27 09.72	+34 08 11.4	35	17	−0.94
	B0221.6+3406B	02 24 41.08	+34 19 43.6	459	433	−0.93
	...	02 24 41.106	+34 19 41.88	78	382	...
	B0221.6+3406	02 24 39.96	+34 20 03.1	459	543	...
	B0223.9+3351	02 26 55.50	+34 04 55.7	532	525	−1.02
	...	02 26 55.564	+34 04 55.57	114	269	...
	B0221.6+3406A	02 24 34.48	+34 21 39.5	104	109	−1.11
	...	02 24 34.514	+34 21 35.03	97	84	...
	B0224.8+3406	02 27 54.18	+34 19 39.5	83	73	−0.88
	B0221.3+3405	02 24 20.16	+34 19 17.5	195	193	−0.84
	B0224.9+3419	02 27 59.75	+34 32 46.5	50	33	0.15
	B0224.2+3430	02 27 16.40	+34 43 42.9	129	128	−0.96
0.5° – 1°	B0220.7+3401	02 23 47.53	+34 15 08.3	403	421	−0.80
	B0225.5+3419A	02 28 29.29	+34 34 43.2	89	75	−0.33
	B0225.5+3419	02 28 34.05	+34 33 09.5	504	568	−1.06
	B0225.5+3419B	02 28 34.63	+34 32 58.5	504	492	−0.97
	B0223.2+3441	02 26 17.12	+34 54 36.5	88	85	−0.71
	...	02 26 17.184	+34 54 36.40	126	119	...
	B0224.8+3434	02 27 51.46	+34 47 36.1	100	99	−0.65
	B0223.5+3443	02 26 36.80	+34 56 42.9	38	33	−0.39
	B0225.5+3347	02 28 34.76	+34 01 00.2	148	139	−0.71
	B0224.7+3442	02 27 43.89	+34 56 23.1	100	85	−0.90
	B0221.0+3440	02 24 03.11	+34 54 26.6	107	102	−0.41
	B0225.7+3340	02 28 45.59	+33 53 31.1	95	84	−0.66
	B0220.4+3433	02 23 25.14	+34 47 20.1	134	145	...
	B0219.6+3404	02 22 40.67	+34 18 10.7	54	41	−0.87
	B0225.8+3438A	02 28 48.50	+34 51 32.8	87	86	−0.85
	B0219.6+3415	02 22 38.27	+34 29 29.1	188	174	−0.81
	B0225.8+3438	02 28 52.37	+34 52 17.3	87	161	...
	B0225.8+3438B	02 28 56.96	+34 53 04.5	81	74	−0.92
	B0219.8+3343A	02 22 48.79	+33 57 18.9	638	638	−0.83
	B0219.8+3343	02 22 48.85	+33 57 11.3	638	688	−0.88
	B0221.2+3325	02 24 11.73	+33 39 18.1	185	178	−0.78
	B0219.8+3343B	02 22 49.91	+33 55 04.3	49	49	−0.84
	B0218.8+3402	02 21 50.01	+34 16 19.1	359	347	−0.88
	B0223.5+3501	02 26 32.36	+35 15 21.8	122	102	−0.81
	B0218.9+3353	02 21 56.58	+34 07 17.5	127	122	−0.92
	B0227.5+3414	02 30 35.36	+34 27 45.3	74	67	−0.86
	B0219.2+3339	02 22 16.75	+33 53 27.3	516	499	−0.67



Table 3—Continued

Annulus	WENSS Source	R.A. (J2000.0)	Decl. (J2000.0)	$S_P$ (mJy beam <sup>-1</sup> )	$S_I$ (mJy)	$\alpha$
	...	02 22 16.812	+33 53 26.90	251	417	...
	B0227.0+3335	02 30 01.40	+33 48 48.3	142	138	...
1° – 1.5°	B0218.6+3342	02 21 40.00	+33 56 36.1	195	204	−0.84
	B0227.6+3343	02 30 41.94	+33 56 23.3	68	59	−0.35
	B0225.4+3312	02 28 25.15	+33 26 14.0	128	111	−0.63
	B0226.5+3321	02 29 31.62	+33 34 23.8	215	207	−0.79
	B0218.1+3419	02 21 09.69	+34 33 37.8	252	252	−0.54
	B0220.5+3310	02 23 33.90	+33 24 35.5	179	175	−0.80
	B0227.7+3443	02 30 44.68	+34 57 14.6	98	96	−0.53
	B0227.3+3325	02 30 19.97	+33 38 53.8	76	68	−0.80
	B0219.1+3323	02 22 06.57	+33 36 49.0	123	112	−0.88
	B0224.6+3515	02 27 38.33	+35 28 43.8	164	147	−0.82
	B0227.7+3324	02 30 42.60	+33 37 59.8	1029	996	−0.77
	B0226.1+3509	02 29 11.30	+35 22 22.6	160	178	...
	B0217.9+3442	02 20 56.23	+34 56 36.2	94	104	−0.72
	B0225.0+3258	02 28 03.91	+33 11 27.5	399	388	−0.96
	B0228.9+3429	02 31 59.53	+34 42 26.7	2361	2556	−1.02
	B0227.9+3322	02 30 56.80	+33 35 16.5	477	433	−0.77
	B0225.5+3255	02 28 30.73	+33 09 16.4	161	131	−0.68
	B0229.4+3410	02 32 28.67	+34 24 03.0	9334	9459	−0.88
	B0217.8+3452B	02 20 49.19	+35 06 28.3	107	98	−1.30
	B0217.8+3452	02 20 48.92	+35 06 25.2	107	109	−1.37
	B0216.6+3409	02 19 37.82	+34 23 10.5	555	515	−1.06
	B0229.0+3332	02 32 05.82	+33 45 22.2	321	305	−1.24
	B0220.8+3527	02 23 50.17	+35 41 31.7	398	393	−0.83
	B0216.2+3405B	02 19 18.40	+34 19 49.5	273	338	...
	B0216.2+3405	02 19 15.49	+34 19 42.1	412	802	...
	B0216.8+3334	02 19 48.77	+33 48 16.0	1352	1357	...
	B0229.3+3447	02 32 21.61	+35 01 06.8	352	381	−1.30
	B0216.2+3405A	02 19 13.44	+34 19 37.2	412	463	...
1.5° – 2°	B0230.3+3429	02 33 20.42	+34 42 54.1	170	172	0.06
	B0229.3+3318	02 32 21.28	+33 32 08.4	168	150	−0.77
	B0223.5+3542	02 26 36.14	+35 55 46.2	1758	1730	−0.59
	...	02 26 36.114	+35 55 45.44	675	1491	...
	B0226.2+3534	02 29 20.00	+35 47 40.2	167	163	−0.80
	B0220.1+3238	02 23 09.03	+32 51 58.0	206	257	...
	B0220.1+3238A	02 23 08.00	+32 51 43.3	206	191	−0.77
	B0216.2+3318	02 19 11.54	+33 31 49.9	302	284	−0.53
	B0229.4+3517	02 32 29.32	+35 30 53.6	2149	2359	−0.86
	B0231.2+3500	02 34 15.22	+35 13 53.0	294	300	−0.95
	B0219.6+3547	02 22 37.70	+36 01 01.1	487	515	−0.93
	B0218.0+3542	02 21 05.40	+35 56 13.0	2534	2460	−0.25
	B0232.4+3405	02 35 26.28	+34 18 30.3	391	384	−0.55
	B0214.7+3321	02 17 43.31	+33 35 03.0	683	657	−0.85
	B0223.0+3603	02 26 04.82	+36 17 10.0	337	355	−1.11

Table 3—Continued

Annulus	WENSS Source	R.A. (J2000.0)	Decl. (J2000.0)	$S_P$ (mJy beam <sup>-1</sup> )	$S_I$ (mJy)	$\alpha$
2° – 3°	B0223.0+3603A	02 26 04.43	+36 17 19.8	337	308	–1.02
	B0214.5+3503	02 17 35.04	+35 17 22.6	1146	1092	...
	B0217.8+3227	02 20 48.04	+32 41 07.0	1415	1393	–0.28
	B0230.1+3243	02 33 12.09	+32 56 48.5	594	606	–0.98
	B0230.1+3243B	02 33 12.37	+32 56 51.2	594	572	–0.94
	B0215.4+3536	02 18 28.69	+35 49 58.6	1445	1401	–0.89
	B0227.2+3206B	02 30 16.48	+32 20 27.1	642	685	...
	B0227.2+3206	02 30 14.54	+32 19 48.0	713	1473	...
	B0227.2+3206A	02 30 12.82	+32 19 12.7	713	788	–1.06
	B0233.2+3458	02 36 19.28	+35 11 15.2	871	843	–0.97
	B0211.9+3452	02 14 58.14	+35 06 39.5	3011	3084	–0.83
	B0224.9+3650	02 28 01.68	+37 03 36.3	1409	1455	–0.90
	B0225.1+3659	02 28 13.67	+37 12 57.1	1566	1519	–1.09

Note. — Units of right ascension are hours, minutes and seconds, and units of declination are degree, arcminutes and arcseconds. The first data entry for each target refers to the WENSS target source, and the second entry, when present, refers to the VLBI detection. The spectral index  $\alpha$  is defined as  $S_\nu \propto \nu^\alpha$  and is estimated from the WENSS and NVSS integrated flux densities where available.

Table 4. Astrometry and Photometry at 324 MHz for field 2 targets.

Annulus	WENSS Source	R.A. (J2000.0)	Decl. (J2000.0)	$S_P$ (mJy beam <sup>-1</sup> )	$S_I$ (mJy)	$\alpha$
0° – 0.25°	B0218.0+3542	02 21 05.40	+35 56 13.0	2534	2460	−0.25
	...	02 21 05.4720	+35 56 13.716	90	1320	...
	B0218.8+3545	02 21 55.21	+35 59 20.4	20	22	−0.90
0.25° – 0.5°	B0219.1+3533	02 22 10.16	+35 46 48.3	89	87	−1.08
	...	02 22 10.123	+35 46 51.67	48	85	...
	B0219.6+3547	02 22 37.70	+36 01 01.1	487	515	−0.93
	B0217.3+3600	02 20 23.66	+36 14 36.8	174	178	−0.96
	B0219.6+3533	02 22 37.61	+35 47 30.9	20	19	−1.02
	B0216.9+3526	02 19 57.00	+35 40 41.9	31	32	−1.33
	B0218.8+3604	02 21 55.81	+36 17 49.5	32	29	−1.18
	B0218.5+3518	02 21 34.18	+35 32 12.5	58	44	−0.78
	B0216.6+3523	02 19 42.13	+35 37 43.9	48	59	−0.24
	...	02 19 42.305	+35 37 44.33	41	84	...
	B0216.2+3555	02 19 18.61	+36 08 59.4	23	21	...
	B0220.0+3552	02 23 06.20	+36 06 06.5	22	36	...
	B0220.1+3532	02 23 10.75	+35 45 50.0	80	76	−0.75
	...	02 23 10.747	+35 45 46.65	53	97	...
	B0215.9+3553	02 19 00.18	+36 07 34.5	22	14	−0.12
	B0219.8+3524	02 22 52.98	+35 38 26.2	29	29	−0.64
	B0220.3+3537	02 23 23.98	+35 51 05.8	35	33	−0.50
	B0217.4+3610	02 20 26.67	+36 24 39.8	22	29	−0.88
0.5° – 1°	B0220.4+3531	02 23 27.04	+35 45 29.4	25	23	−0.32
	B0216.7+3515A	02 19 44.91	+35 30 18.8	18	18	...
	B0216.7+3515	02 19 47.22	+35 29 00.0	48	60	...
	B0216.7+3515B	02 19 47.92	+35 28 32.8	48	41	−1.02
	B0215.4+3536	02 18 28.69	+35 49 58.6	1445	1401	−0.89
	...	02 18 28.996	+35 50 01.84	93	670	...
	B0220.5+3554	02 23 36.81	+36 08 34.1	28	24	−0.83
	B0220.7+3551	02 23 46.60	+36 05 01.3	176	173	−0.97
	...	02 23 46.790	+36 05 03.20	104	149	...
	B0219.9+3514	02 22 56.36	+35 28 05.4	26	23	−0.73
	B0220.7+3558A	02 23 47.14	+36 11 34.5	85	89	−0.79
	B0220.7+3558	02 23 47.37	+36 12 17.3	85	137	...
	B0220.8+3527	02 23 50.17	+35 41 31.7	398	393	−0.83
	B0220.7+3558B	02 23 47.92	+36 13 49.8	45	47	−0.93
	B0221.1+3548	02 24 08.54	+36 01 55.2	40	34	−1.06
	B0221.1+3551	02 24 13.51	+36 04 51.9	73	67	−0.86
	B0220.5+3609	02 23 32.65	+36 22 47.7	22	22	...
	B0215.2+3522	02 18 13.64	+35 36 42.5	42	39	−0.80
	B0215.4+3516	02 18 29.78	+35 30 27.7	110	101	−1.02
	B0219.1+3503	02 22 07.70	+35 17 26.9	73	66	−0.95
	B0221.4+3535A	02 24 26.91	+35 48 50.9	26	19	−0.94
	B0217.8+3500	02 20 50.30	+35 14 26.9	52	38	−0.41
	B0221.4+3535	02 24 29.69	+35 49 01.3	26	38	...
	B0219.2+3622	02 22 18.62	+36 35 49.7	61	89	...

Table 4—Continued

Annulus	WENSS Source	R.A. (J2000.0)	Decl. (J2000.0)	$S_P$ (mJy beam <sup>-1</sup> )	$S_I$ (mJy)	$\alpha$
	B0216.5+3504	02 19 34.57	+35 18 02.7	29	25	−1.08
	B0221.4+3535B	02 24 32.69	+35 49 11.6	26	18	−0.72
	B0216.7+3502	02 19 44.76	+35 16 08.4	26	31	−1.06
	B0215.8+3616	02 18 53.75	+36 30 35.9	126	119	−0.81
	B0214.4+3534	02 17 29.52	+35 47 56.3	105	111	−0.74
	B0217.4+3629	02 20 30.75	+36 42 48.3	58	48	−0.52
	B0219.6+3625	02 22 43.74	+36 39 02.3	34	24	−0.88
	B0220.5+3618	02 23 38.39	+36 32 08.0	30	21	−0.19
	B0213.9+3543	02 16 59.68	+35 57 21.6	162	179	−0.72
	B0218.5+3632	02 21 32.74	+36 45 45.5	54	63	−0.75
	B0217.8+3452B	02 20 49.19	+35 06 28.3	107	98	...
	B0217.8+3452	02 20 48.92	+35 06 25.2	107	109	...
	B0218.9+3452	02 21 57.11	+35 06 09.7	37	30	−0.6
	B0215.8+3626	02 18 49.99	+36 40 41.6	156	144	−0.07
	...	02 18 50.038	+36 40 42.58	101	126	...
	B0222.4+3543	02 25 28.81	+35 57 10.2	108	89	−0.68
	B0213.6+3540	02 16 37.63	+35 54 21.1	224	234	−1.03
	B0222.6+3554	02 25 40.74	+36 08 19.9	48	74	...
	B0222.6+3554B	02 25 42.54	+36 07 28.8	48	45	−0.54
	B0221.4+3622	02 24 31.52	+36 36 02.1	33	51	−0.60
	B0214.5+3503	02 17 35.04	+35 17 22.6	1146	1092	−0.90
	...	02 17 34.989	+35 17 21.49	187	808	...
	B0214.1+3507	02 17 11.78	+35 21 05.3	81	81	−0.73
	B0217.9+3442	02 20 56.23	+34 56 36.2	94	104	−0.72
1° – 1.5°	B0222.4+3613A	02 25 29.65	+36 25 50.9	60	91	...
	B0222.4+3613	02 25 30.21	+36 26 34.7	99	185	...
	B0222.4+3613B	02 25 30.65	+36 27 08.9	99	93	−0.77
	B0213.1+3558	02 16 09.27	+36 12 34.7	44	37	−0.67
	B0223.1+3551	02 26 10.41	+36 04 41.9	33	29	...
	B0215.4+3636	02 18 30.87	+36 50 27.2	339	321	−0.55
	...	02 18 30.913	+36 50 27.45	127	136	...
	B0212.9+3535	02 15 55.24	+35 49 12.0	61	64	−0.68
	B0222.4+3617	02 25 29.56	+36 31 03.3	64	57	−0.85
	B0217.3+3645	02 20 20.42	+36 59 16.7	367	2686	...
	B0223.0+3603A	02 26 04.43	+36 17 19.8	337	308	−1.02
	B0223.0+3603	02 26 04.82	+36 17 10.0	337	355	−1.11
	B0213.9+3502	02 16 57.40	+35 16 33.5	61	64	−0.77
	B0223.0+3603B	02 26 08.11	+36 15 47.6	50	47	...
	B0212.8+3553	02 15 48.66	+36 06 56.9	83	79	−0.80
	B0212.9+3603	02 15 57.29	+36 16 55.4	93	91	−0.82
	B0222.7+3618	02 25 45.12	+36 31 32.5	57	57	−0.81
	B0223.5+3542	02 26 36.14	+35 55 46.2	1758	1730	−0.59
	...	02 26 36.104	+35 55 45.53	518	954	...
	B0217.0+3648B	02 20 08.92	+37 02 21.4	42	54	−1.11
	B0217.0+3648	02 20 06.68	+37 02 41.2	45	95	...

Table 4—Continued

Annulus	WENSS Source	R.A. (J2000.0)	Decl. (J2000.0)	$S_P$ (mJy beam <sup>-1</sup> )	$S_I$ (mJy)	$\alpha$
	B0217.0+3648A	02 20 04.01	+37 03 08.9	45	40	−0.69
	B0217.4+3434	02 20 29.93	+34 48 25.1	62	57	−1.08
	B0213.0+3614B	02 16 02.26	+36 27 54.2	98	94	−0.81
	B0213.0+3614	02 16 01.21	+36 27 59.1	98	117	...
	B0222.6+3623	02 25 44.67	+36 36 36.7	171	158	−0.55
	B0223.7+3600	02 26 46.21	+36 13 50.2	45	36	−0.53
	B0223.8+3533	02 26 54.06	+35 47 03.2	48	45	−0.89
	...	02 26 53.435	+35 46 48.08	86	90	...
	B0221.0+3440	02 24 03.11	+34 54 26.6	107	102	−0.41
	B0223.6+3607	02 26 43.34	+36 20 55.7	109	100	−0.57
	B0212.2+3604	02 15 18.14	+36 17 57.2	1278	1303	−0.96
	B0220.4+3433	02 23 25.14	+34 47 20.1	134	145	−0.98
	B0224.3+3544	02 27 23.05	+35 57 42.5	72	75	−0.67
	B0216.3+3656	02 19 21.87	+37 10 05.7	106	98	−0.77
	B0223.5+3501	02 26 32.36	+35 15 21.8	122	102	−0.81
	B0216.6+3659	02 19 40.76	+37 13 05.2	82	89	−0.61
	B0218.1+3419	02 21 09.69	+34 33 37.8	252	252	−0.54
	B0224.7+3558	02 27 48.73	+36 11 25.1	61	47	−0.02
	B0211.2+3550	02 14 14.41	+36 04 40.5	182	186	−0.84
	B0212.4+3454	02 15 24.71	+35 08 50.6	78	66	−0.86
	B0224.6+3515	02 27 38.33	+35 28 43.8	164	147	−0.82
	B0222.3+3650	02 25 22.43	+37 03 40.9	146	172	−0.95
	B0220.0+3704	02 23 07.86	+37 18 03.6	200	198	−0.82
	B0224.8+3607A	02 27 51.15	+36 21 29.6	97	98	−1.23
	B0224.8+3607	02 27 52.76	+36 21 01.3	97	168	...
	B0224.8+3607B	02 27 54.99	+36 20 24.2	88	69	−0.79
	B0214.1+3430	02 17 05.91	+34 44 30.4	128	136	−0.82
	B0211.5+3505	02 14 29.85	+35 19 20.0	213	232	...
	B0223.2+3441	02 26 17.12	+34 54 36.5	88	85	−0.71
	B0224.7+3617	02 27 50.29	+36 30 47.1	200	178	−0.82
	B0219.6+3415	02 22 38.27	+34 29 29.1	188	174	−0.81
	B0211.2+3511	02 14 13.61	+35 25 07.2	357	359	−0.91
	B0211.0+3518	02 14 01.38	+35 32 28.7	174	189	−0.73
	B0211.9+3452	02 14 58.14	+35 06 39.5	3011	3084	−0.83
	...	02 14 57.959	+35 06 32.27	259	869	...
1.5° – 2°	B0210.7+3533	02 13 43.25	+35 47 29.5	149	141	−0.97
	B0214.3+3700	02 17 22.91	+37 14 47.8	669	650	−1.18
	...	02 17 22.726	+37 14 47.08	207	248	...
	B0222.3+3656	02 25 27.31	+37 10 27.9	373	380	−0.45
	B0216.0+3413	02 19 01.20	+34 27 45.7	131	136	−0.66
	B0225.0+3620	02 28 07.42	+36 34 09.5	227	235	−0.83
	B0216.6+3409	02 19 37.82	+34 23 10.5	555	515	−1.06
	B0215.1+3710	02 18 11.43	+37 24 36.5	481	473	−0.70
	...	02 18 11.421	+37 24 35.44	184	192	...
	B0223.9+3646	02 26 59.91	+36 59 27.9	76	60	−0.75

Table 4—Continued

Annulus	WENSS Source	R.A. (J2000.0)	Decl. (J2000.0)	$S_P$ (mJy beam <sup>-1</sup> )	$S_I$ (mJy)	$\alpha$
	B0219.2+3717	02 22 15.42	+37 31 16.7	144	123	−0.08
	B0225.9+3602	02 28 57.74	+36 16 13.8	125	122	−0.80
	B0212.8+3429	02 15 49.40	+34 43 02.8	213	199	−0.19
	B0221.9+3417	02 24 56.18	+34 30 35.8	1657	1638	−0.91
	...	02 24 56.629	+34 30 27.43	184	222	...
	B0211.1+3634	02 14 11.25	+36 48 24.9	228	244	−1.20
	B0216.2+3405B	02 19 18.40	+34 19 49.5	273	338	−0.96
	B0216.2+3405	02 19 15.49	+34 19 42.1	412	802	...
	B0216.2+3405A	02 19 13.44	+34 19 37.2	412	463	−0.86
	B0218.8+3402	02 21 50.01	+34 16 19.1	359	347	−0.88
	B0226.2+3534	02 29 20.00	+35 47 40.2	167	163	−0.80
	B0224.7+3442	02 27 43.89	+34 56 23.1	100	85	−0.90
	B0221.6+3406A	02 24 34.48	+34 21 39.5	104	109	−1.11
	B0209.5+3536	02 12 31.09	+35 50 40.1	381	482	...
	B0226.1+3509	02 29 11.30	+35 22 22.6	160	178	...
	B0224.2+3430	02 27 16.40	+34 43 42.9	129	128	−0.96
	B0221.3+3405	02 24 20.16	+34 19 17.5	195	193	−0.84
	B0221.6+3406	02 24 39.96	+34 20 03.1	459	543	...
	B0221.6+3406B	02 24 41.08	+34 19 43.6	459	433	−0.93
	B0220.7+3401	02 23 47.53	+34 15 08.3	403	421	−0.80
	B0226.3+3619	02 29 24.87	+36 32 26.6	191	174	−0.85
	B0224.9+3650	02 28 01.68	+37 03 36.3	1409	1455	−0.90
	B0226.5+3618	02 29 35.60	+36 31 22.9	417	401	−0.67
	...	02 29 35.650	+36 31 24.65	294	335	...
	B0218.9+3353	02 21 56.58	+34 07 17.5	127	122	−0.92
	B0216.9+3732	02 19 59.02	+37 45 56.1	373	362	−0.78
	B0223.1+3408	02 26 10.15	+34 21 30.7	3793	3678	−0.16
	...	02 26 10.338	+34 21 30.28	700	1834	...
	B0212.4+3714	02 15 31.32	+37 28 43.3	333	323	−0.71
	B0209.2+3504	02 12 14.34	+35 18 24.7	253	230	−0.85
	B0225.1+3659	02 28 13.67	+37 12 57.1	1566	1519	−1.09
	...	02 28 13.706	+37 12 58.23	643	692	...
	B0208.4+3547	02 11 28.80	+36 01 26.2	446	431	−0.94
	B0210.3+3652	02 13 22.53	+37 07 00.0	303	320	...
	B0225.6+3655	02 28 42.20	+37 08 58.0	306	308	−0.85
	B0225.6+3655A	02 28 42.07	+37 09 03.6	306	286	−0.80
	B0212.5+3405	02 15 29.49	+34 19 47.5	337	328	−0.86
2° – 3°	B0218.6+3342	02 21 40.00	+33 56 36.1	195	204	−0.84
	B0219.8+3343A	02 22 48.79	+33 57 18.9	638	638	−0.83
	B0219.8+3343	02 22 48.85	+33 57 11.3	638	688	−0.88
	B0228.1+3547	02 31 11.57	+36 00 28.4	321	303	−1.33
	B0219.2+3339	02 22 16.75	+33 53 27.3	516	499	−0.67
	...	02 22 16.801	+33 53 26.98	331	337	...
	B0225.5+3419	02 28 34.05	+34 33 09.5	504	568	−1.06
	B0225.5+3419B	02 28 34.63	+34 32 58.5	504	492	−0.97

Table 4—Continued

Annulus	WENSS Source	R.A. (J2000.0)	Decl. (J2000.0)	$S_P$ (mJy beam <sup>-1</sup> )	$S_I$ (mJy)	$\alpha$
	B0216.8+3334	02 19 48.77	+33 48 16.0	1352	1357	−0.81
	B0212.6+3736	02 15 40.01	+37 50 09.3	691	655	−0.54
	B0223.9+3351	02 26 55.50	+34 04 55.7	532	525	−1.02
	B0208.9+3429	02 11 54.12	+34 44 01.7	569	551	−1.08
	B0210.5+3404	02 13 28.47	+34 18 20.0	402	482	−0.90
	B0216.0+3756B	02 19 09.03	+38 10 00.7	439	645	−0.84
	B0216.0+3756	02 19 08.14	+38 10 15.6	439	739	...
	B0206.6+3533	02 09 38.91	+35 47 48.9	4259	5519	−0.67
	B0206.6+3533A	02 09 38.87	+35 47 48.9	4259	5489	−0.66
	B0213.2+3750	02 16 19.76	+38 04 39.4	709	782	−0.89
	B0229.4+3517	02 32 29.32	+35 30 53.6	2149	2359	−0.86
	B0227.3+3713	02 30 25.65	+37 26 18.0	1034	1013	−1.10
	B0214.7+3321	02 17 43.31	+33 35 03.0	683	657	−0.85
	B0228.9+3429	02 31 59.53	+34 42 26.7	2361	2556	−1.02
	B0228.1+3729	02 31 14.98	+37 42 57.0	1426	1397	−1.03
	B0229.4+3410	02 32 28.67	+34 24 03.0	9334	9459	−0.88

Note. — Units of right ascension are hours, minutes and seconds, and units of declination are degree, arcminutes and arcseconds. The first data entry for each target refers to the WENSS target source, and the second entry, when present, refers to the VLBI detection. The spectral index  $\alpha$  is defined as  $S_\nu \propto \nu^\alpha$  and is estimated from WENSS and NVSS integrated flux densities where available.

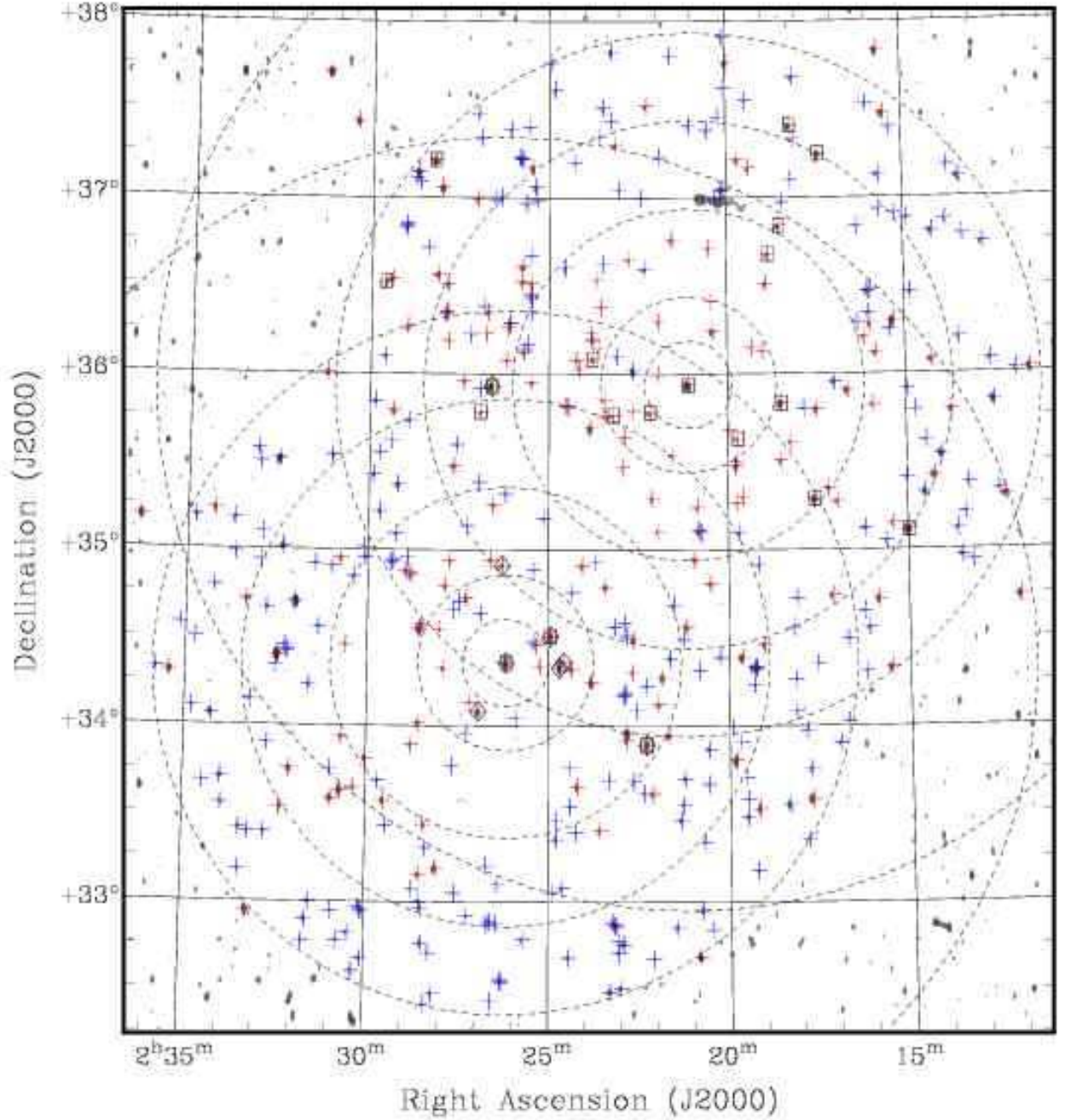


Fig. 1.— Gray-scale WENSS image of the two fields surveyed by the VLBA, JB and WB VLBI observation. The dashed circles define the six sub-fields that are co-located on the phase centre of each field of the VLBI observation. The crosses located across the image denote all WENSS sources that were targeted by the VLBI observation, red crosses mark unresolved WENSS sources with peak flux densities above the VLBI sensitivity limit and green crosses mark sources that were resolved in WENSS or fell below the VLBI sensitivity limit. Targets that are boxed identify VLBI sources detections in the B0218+357 field and those that are contained within a diamond identify VLBI detections in the J0226+3421 field. The four sources that were commonly detected within both of the fields and are marked within a box and diamond.



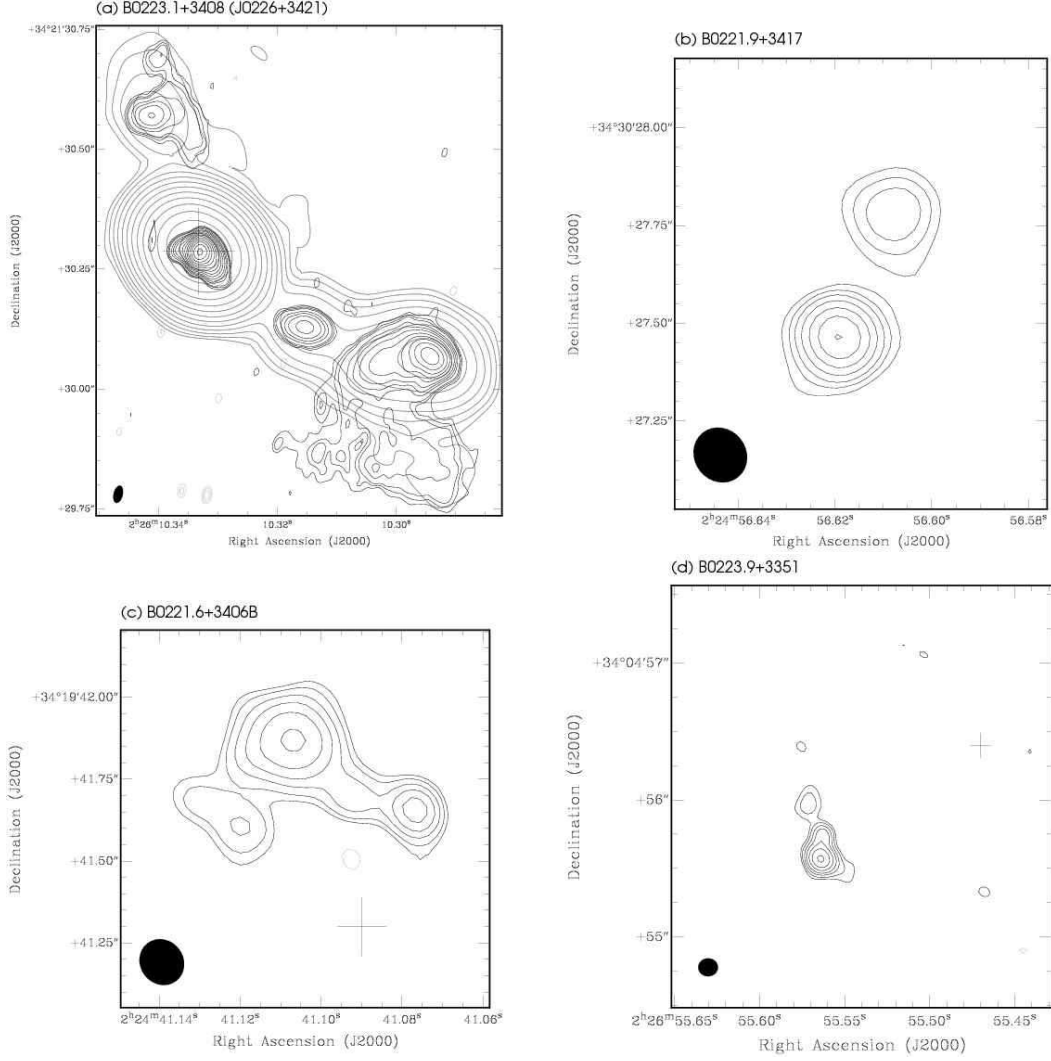


Fig. 2.— Naturally weighted VLBI images of field 1 sources. Contours are drawn at  $\pm 2^0, \pm 2^{\frac{1}{2}}, \pm 2^1, \pm 2^{\frac{3}{2}}, \dots$  times the  $3\sigma$  rms noise except for B0223.1+3408 where the lowest contour is at  $1.5\sigma$  rms noise. Restoring beam and rms image noise for all images can be found in Table 2. Crosses mark the best known radio positions (see Table 2). Notes for sub-figures (a) Grey contours: 2 cm VLA + Pie Town contour map;  $1\sigma$  RMS noise is  $0.053 \text{ mJy beam}^{-1}$ ; contours at  $\pm 1, \pm 2, \pm 4, \pm 8, \dots$  times the  $3\sigma$  rms noise; beam size is  $118 \times 96 \text{ mas}$  at P.A. =  $51^\circ$ ; (h) Grey contours: Field 2 detection of source restored using the same beam as the field 1 source.

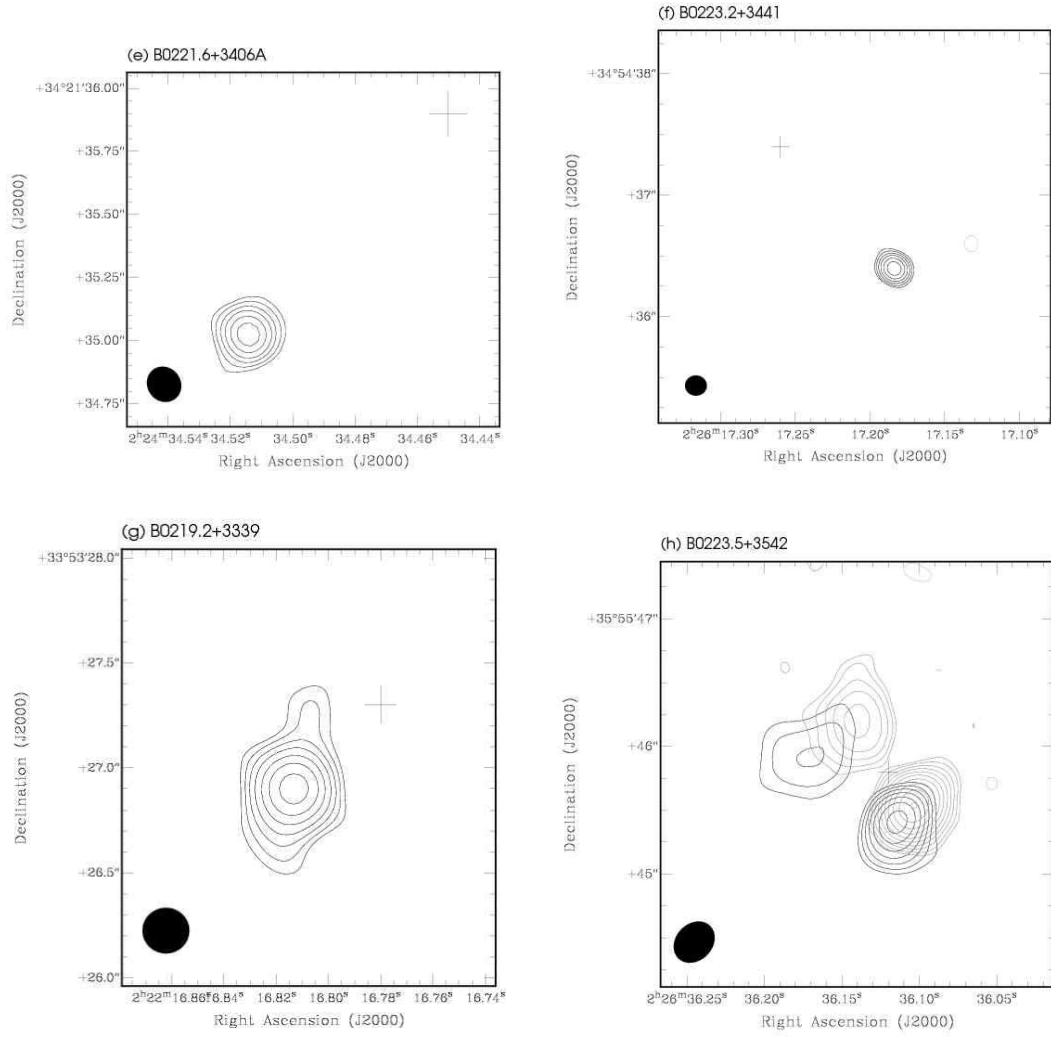


Fig. 2. — Continued

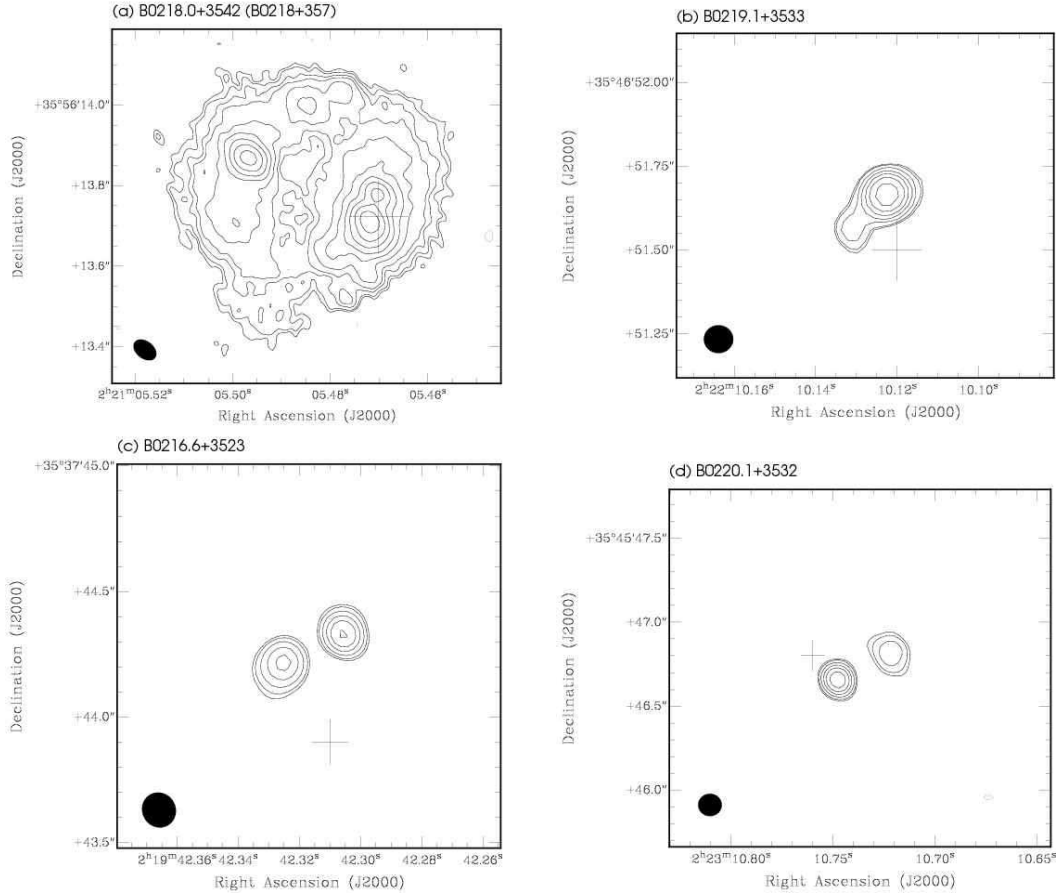


Fig. 3.— Naturally weighted VLBI images of field 2 sources. Contours are drawn at  $\pm 2^0, \pm 2^{\frac{1}{2}}, \pm 2^1, \pm 2^{\frac{3}{2}}, \dots$  times the  $3\sigma$  rms noise. Restoring beam and rms image noise for all images can be found in Table 2. Crosses mark the best known radio positions (see Table 2). Notes for sub-figures (e) and (h) Grey contours: 1465 MHz VLA contour map (Röttgering et al. 1994); (o), (q) and (s) Grey contours: Field 1 detection of source restored using the same beam as the field 2 source.

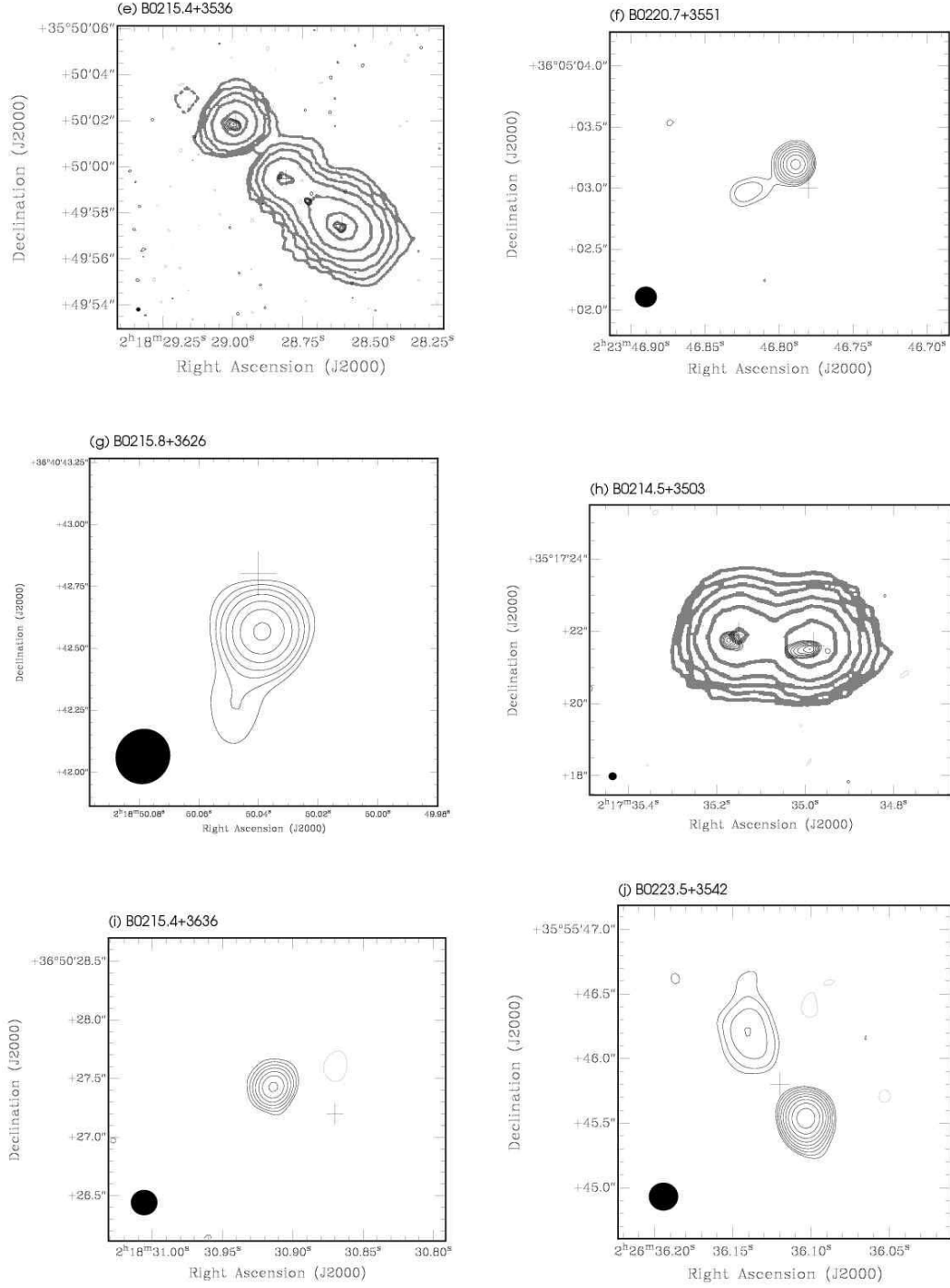


Fig. 3. — Continued

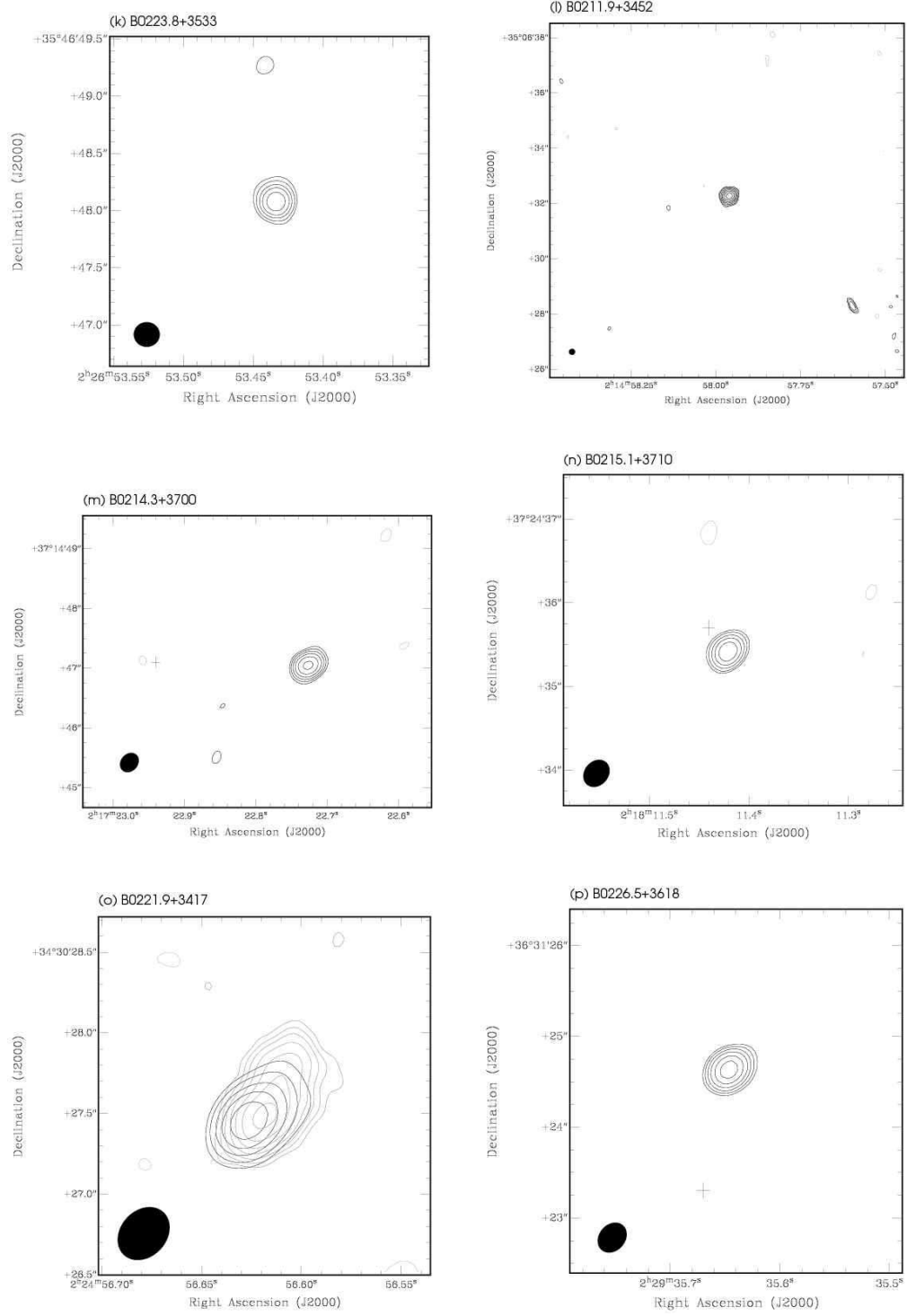


Fig. 3. — Continued

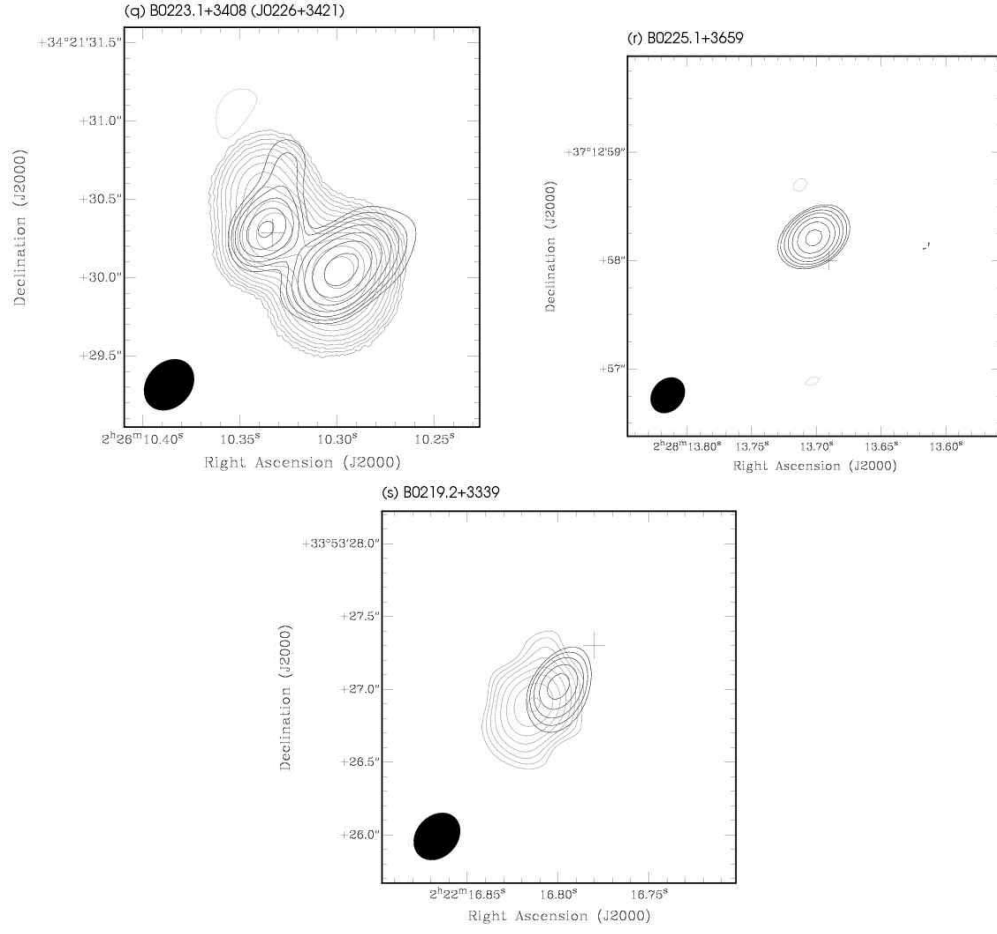


Fig. 3. — Continued

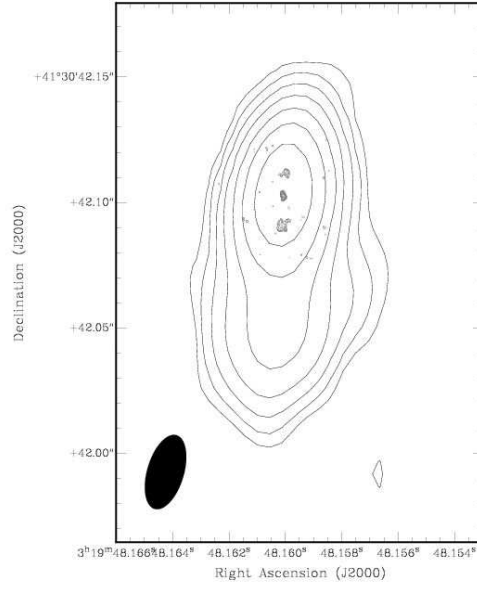


Fig. 4.— Naturally weighted VLBI image of 3C84. Contours drawn at  $\pm 1, \pm 2, \pm 4, \dots$  times the  $3\sigma$  rms noise. Restoring beam and rms image noise for all images can be found in Table 2. A 15 GHz VLBA contour map is shown in grey (Lister, & Homan 2005) with a peak flux density of  $2.65 \text{ Jy beam}^{-1}$  and an integrated flux of 10.64 Jy. Contours are shown at 10, 20, 40, 80,  $\dots$ , 2560 mJy  $\text{beam}^{-1}$  and the restoring beam is  $0.69 \times 0.55 \text{ mas}$  at a position angle of  $2^\circ$ .